Distinct evolutions of haze pollution from winter to following spring over the North China Plain: Role of the North Atlantic sea surface temperature anomalies

Linye Song[1], Shangfeng Chen[2*], Wen Chen[2], Jianping Guo[3], Conglan Cheng[1], and Yong Wang[4]

[1]*Institute of Urban Meteorology, China Meteorological Administration, Beijing, China*

[2]*Center for Monsoon System Research, Institute of Atmospheric Physics, Chinese Academy of Sciences, Beijing, China*

[3]*State Key Laboratory of Severe Weather, Chinese Academy of Meteorological Sciences, Beijing, China*

[4]*ZAMG, Central Institute for Meteorology and Geodynamics, Vienna, Austria*

Atmospheric Chemistry and Physics

Submitted in March 2021

Revised in November 2021

Corresponding authors:

Dr. Shangfeng Chen

E-mail: chenshangfeng@mail.iap.ac.cn

Abstract

This study reveals that haze pollution (HP) over the North China Plain (NCP) in winter can persist to following spring during most years. The persistence of HP_{NCP} is attributed to maintenance of an anticyclonic anomaly (AA) over northeast Asia and southerly wind anomalies over the NCP. Southerly wind anomalies over the NCP reduce surface wind speed and increase relative humidity, which are conducive to above-normal HP_{NCP} both in winter and spring. However, there exist several years when above-normal HP_{NCP} in winter are followed by below-normal HP_{NCP} in the following spring. The reversed HP_{NCP} in winter and spring in these years is due to the inverted atmospheric anomalies over northeast Asia. In particular, AA over northeast Asia in winter is replaced by a cyclonic anomaly (CA) in the following spring. The resultant spring northerly wind anomalies over NCP are conducive to below-normal HP_{NCP}. These two distinctive evolutions of HP_{NCP} and atmospheric anomalies over northeast Asia from winter to spring are attributed to the different evolutions of sea surface temperature anomalies (SSTA) in the North Atlantic. In the persistent years, warm North Atlantic SSTA in winter maintains to following spring via positive air-sea interaction process and induces a negative spring North Atlantic Oscillation (NAO)-like pattern, which contributes to the AA over northeast Asia via atmospheric wave train. By contrast, in the reverse years, cold SSTA in the North Atlantic is maintained from winter to spring, which induces a positive spring NAO-like pattern and leads to CA over northeast Asia via atmospheric wave train. Hence, this study improves our understanding of the characteristic of haze pollution evolution from

winter to the following spring, and suggests the potential role of North Atlantic SSTA to be served as an important preceding signal for haze pollution prediction by one-season ahead over the North China Plain.

Keywords: Evolution of Haze pollution; North China Plain; North Atlantic sea surface temperature; North Atlantic Oscillation; Atmospheric circulation

1. Introduction

Haze pollution has become a serious air quality issue in China accompanying the rapid urbanization and fast economic development (e.g. Ding and Liu 2004; Wang and Chen 2016; Zhang et al. 2018). It has been well recognized that the occurrence of haze pollution events can exert substantial impacts on the human health, air transportation, ground traffic, agriculture production, and regional climate change (e.g. Koren et al. 2012; Zhang and Crooks 2012; Fu et al. 2014; Wang et al. 2014a, 2014b; Wu et al. 2016; Tie et al. 2016; Cohen et al. 2017; Guo et al. 2018; Zhang et al. 2018; Lu et al. 2019). For example, Cohen et al. (2017) reported that near 4.2 million premature deaths in the world in 2015 were attributed to the overexposure of PM2.5. In addition, haze pollution is suggested to result in a decrease of about 1.2%-3.8% of the annual Gross National Product (GNP, Zhang and Crooks 2012). Furthermore, increasing concentration of anthropogenic aerosol, which is related to the enhanced haze pollution, could exert significant impacts on the atmospheric circulation and regional precipitation change (Koren et al. 2012; Wang et al. 2014a). Considering the notable impacts of haze pollution, it is of great scientific importance to improve our understanding of the factors contributing to haze pollution and the associated mechanisms.

A number of previous studies have investigated the factors responsible for the variations of haze pollution in China on multiple timescales. The long-term increasing trend of haze pollution in China is generally attributable to the rapid increases in anthropogenic emissions (e.g. Che et al. 2009; Ding and Liu 2014; Zhao et al. 2016;

Cheng et al. 2019). For example, Zhao et al. (2016) showed that the notable increasing trend of haze pollution in winter over eastern China has a close relationship with the Gross Domestic Product (GDP) in China. Several studies suggested that changes in the meteorological conditions due to global warming also play a role in the long-term trend of haze pollution in China (e.g. Cai et al. 2017; Liu et al. 2017; Ding et al. 2017; Zhang et al. 2020).

On the interannual and interdecadal timescales, variations of the haze pollution in China are suggested to be mainly controlled by the meteorological conditions. For instance, Dang and Liao (2019) reported that the changes of meteorological conditions accounted for about 70% of the variation of the annual haze days in the Beijing-Tianjin-Hebei region. Zhao et al. (2016) suggested that the Pacific Decadal Oscillation could exert marked impacts on the interdecadal variation of the haze pollution in eastern China via inducing large-scale atmospheric circulation anomalies over East Asia. Pacific Decadal Oscillation is the first leading mode of sea surface temperature anomalies (SSTA) in the North Pacific on the interdecadal timescale (Mantua et al., 1997; Zhang et al., 1997; Duan et al. 2013). Xiao et al. (2014) showed that the Atlantic Multidecadal Oscillation modulates haze pollution in China via triggering atmospheric wave train over Eurasia. Atlantic Multidecadal Oscillation is the dominant mode of SSTA in the North Atlantic on the multidecadal timescale (Kerr 2000). Compared to the interdecadal variation, much more studies have examined the factors for the interannual variation of haze pollution in China, mainly concentrating on boreal winter. It is shown that interannual variation of haze pollution in eastern

China can be impacted by the Arctic Oscillation (Yin et al. 2015), East Asian winter Monsoon (Li et al. 2016; Chen et al. 2020), El Niño-Southern Oscillation (Guo and Li 2015; Chang et al. 2016; Liu et al. 2017; Li et al. 2017; He et al. 2019), North Atlantic SSTA (Xiao et al. 2014), Arctic sea ice (Wang et al. 2015; Yin and Wang 2017), Eurasian snow cover (Yin and Wang 2018), and the East Atlantic-Western Russian (EAWR) teleconnection pattern (Yin and Wang 2017; Chen et al. 2020). A recent study has examined the factors modulating the interannual variation of springtime haze pollution in the North China Plain Region (NCPR) (Chen et al. 2019). Note that NCPR is one of the most important regions in China with very dense population, large traffic activities and highly developed economy. In addition, NCPR is also the most polluted region in China (Yin et al. 2015). It is indicated that North Atlantic SSTA and the North Atlantic Oscillation (NAO, the first leading mode of interannual atmospheric variability over the North Atlantic region; Hurrell 1995) play important roles in determining the haze pollution over NCPR via modulating atmospheric circulation anomalies over northeast Asia through triggering atmospheric wave train extending from North Atlantic across Europe to East Asia (Chen et al. 2019). However, Chen et al. (2019) mainly focused on investigating the physical mechanism and was limited to one season of spring. Although there are many previous studies investigating the interannual variations of haze pollution over the NCPR, they mainly separate winter and spring independently. However, impacts of haze pollution may depend strongly on the time period of seasonal persistence. Hence, an important question is raised: whether there exists a relation between interannual variation of

haze pollution over the NCPR in winter and following spring? In particular, could the wintertime haze pollution maintain from winter to the following spring? If so, what are the plausible factors contributing to the across-season persistence of haze pollution over the NCPR from winter to succedent spring? Understanding the evolution features of the haze pollution from winter to spring and the associated mechanisms would have important implications for the seasonal prediction of haze pollution over the NCPR. In this study, the issues raised above will be investigated and addressed.

The remainder of this paper is organized as follows. Section 2 describes the data and methods used in this study. Section 3 examines relation of interannual variations between winter and spring haze pollution over the NCPR, and compares the two distinct types of haze evolutions found in this paper. Section 4 examines the factors responsible for the different evolutions of haze pollution over NCPR from winter to the following spring. Summary and discussion are provided in section 5.

2. Data and methods

2.1 Data

Monthly mean horizontal winds, geopotential height, relative humidity, surface wind speed, surface heat fluxes are obtained from the National Centers for Environmental Prediction-National Center for Atmospheric Research (NCEP-NCAR) reanalysis (Kalnay et al. 1996; https://psl.noaa.gov/data/gridded/data.ncep.reanalysis.html), which are available from

January 1948 to the present. Surface heat fluxes are the sum of the surface latent and sensible heat fluxes, surface shortwave and longwave radiations. Atmospheric data from the NCEP-NCAR reanalysis have a horizontal resolution of 2.5°×2.5° in the longitude-latitude grids, while surface heat fluxes are on T62 Gaussian grids. Monthly mean SST data are derived from the National Oceanic and Atmospheric Administration (NOAA) Extended Reconstructed SST version 5 (ERSSTV5) from January 1854 to the present (Huang et al. 2017; https://psl.noaa.gov/data/gridded/data.noaa.ersst.v5.html), with a horizontal resolution of 2°×2° in the longitude-latitude grids. Atmospheric teleconnection indices, including the EAWR index and NAO index, are provided by the NOAA Climate Prediction Center (https://www.cpc.ncep.noaa.gov/data/).

Surface data of visibility and relative humidity observed at 748 meteorological stations are extracted from the National Meteorological Information Center of China from 1979 to 2012. These meteorological observations are measured daily at 0200, 0800, 1400 and 2000 Beijing time (UTC+8). Following previous studies (Guo et al. 2017; Chen et al. 2019, 2020), a series of quality control techniques are applied to this meteorological data to ensure its quality and consistency. In particular, we exclude the observation station if it contains any missing values throughout the whole analysis period. In addition, the data has been removed when precipitation, snow events, and dust storms occurred. After the above quality control, there remain 218 stations over Eastern China (Fig. 1a). Furthermore, following previous studies (Che et al. 2009; Guo et al. 2017, Chen et al. 2019; 2020), we only use the data at 1400 Beijing time, as

this time may be the most representative of the daily visibility compared to other times. It should be mentioned that the atmospheric visibility, which is traditionally measured by human visual observation, starts to be determined by the automatic visibility instruments since the year 2014. Due to the changes of the observation methods, large uncertainties have emerged due to the issues of heterogeneity as reported by Li et al. (2018). Thus, this study does not employ the visibility data after the 2014.

Long-term trends of all variables have been removed to avoid the impact of the global warming signal and to focus on the interannual variation of haze pollution. Anomalies are calculated by subtracting the monthly climatology from the original data. Significance levels of correlation coefficient and composite differences are estimated based on the two-tailed Student's *t* test.

2.2 Dry Extinction coefficient of aerosol

As in previous studies (Li et al. 2018; Guo et al. 2017; Chen et al. 2019, 2020), this study employs the dry extinction coefficient (DECC) of aerosol to represent the haze pollution. The DECC is defined based on the Koschmieder relationship (Koschmieder 1926):

$$DECC = \frac{K}{Vis_{dry}} \quad (1)$$

where K is equal to 3.912, Vis_{dry} indicates atmospheric visibility after removing the effect of relative humidity. It is noted that atmospheric visibility is not only impacted by the dry particles, but also affected by the amount of water uptake. For instance,

high humidity associated with fog could lead to reduction of atmospheric visibility. Previous studies suggested that the visibility needs to be corrected in the presence of a relative humidity ranging from 40 to 90% (e.g. Rosenfeld et al. 2007), which is expressed as follows:

$$Vis_{dry} = \frac{Vis_{obs}}{0.26 + 0.4285\log(100 - RH)} \quad (2)$$

where Vis_{obs} indicates the observed visibility. Note that all visibility data are discarded when the relative humidity (RH) is higher than 90% to remove the influence of fog events, non-linear aerosol and water interactions (Craig and Faulkenberry 1979; Guo et al. 2017; Chen et al. 2019, 2020).

2.3 Wave activity flux

We use the wave activity flux defined by Takaya and Nakamura (2001) to examine the stationary Rossby wave propagation, which can be expressed as follows:

$$W = \frac{1}{2|\boldsymbol{U}|}\begin{pmatrix} U\left(v'^2 - \psi' v'_x\right) + V\left(-u'v' + \psi' u'_x\right) \\ U\left(-u'v' + \psi' u'_x\right) + V\left(u'^2 + \psi' u'_y\right) \\ \frac{f_o R_a p}{N^2 H_o}\left\{U\left(v'T' - \psi' T'_x\right) + V\left(-u'T' - \psi' T'_y\right)\right\} \end{pmatrix} \quad (3)$$

where $\boldsymbol{U} = (U,V)$ is the climatological wind vector. $\boldsymbol{V} = \left(u',v'\right)$ denotes geostrophic winds anomalies. ψ' is geostrophic stream function anomalies. H_o, p, and N represent scale height, pressure normalized by 1000-hPa, and Brunt-Vaisala frequency, respectively. R_a, T', and f_o denote gas constant of the dry air, air temperature anomalies, and the Coriolis parameter at 45°N, respectively. Subscripts x and y are the derivatives in the zonal and meridional directions, respectively. Climatological mean is calculated over the 1980–2010 period.

2.4 Barotropic model

The present study employs a linear barotropic model to investigate the role of the SST anomalies (SSTA) over the subtropical and tropical North Atlantic in triggering atmospheric Rossby wave train over mid-high latitudes of Eurasia. Previous studies have demonstrated that cold (warm) SSTA in the subtropical and tropical regions are able to induce convergence (divergence) anomalies at the upper-troposphere that act as effective sources of atmospheric stationary Rossby wave (Hodson et al. 2010; Watanabe 2004; Zuo et al. 2013; Wu et al. 2011; Chen et al. 2016, 2020). Based on a simple barotropic vorticity equation (Watanabe 2004; Sardeshmukh and Hoskins 1988; Chen et al. 2020), the barotropic model is established by:

$$\partial_t \nabla^2 \psi' + J\left(\overline{\psi}, \nabla^2 \psi'\right) + J\left(\psi', \nabla^2 \overline{\psi} + f\right) + \alpha \nabla^2 \psi' + \nu \nabla^6 \psi' = S' \qquad (4)$$

where ψ' and $\overline{\psi}$ are the perturbation stream function and basic state stream function, respectively. f and J represent the Coriolis parameter and Jacobian operator, respectively. S' represents the vorticity source generated by the atmospheric divergence. The barotropic model consists a biharmonic diffusion and a linear damping that indicate the Rayleigh friction. Note that solution of the above Equation associated with the barotropic model is determined by the vorticity perturbation (S') and the basic state. In the present analysis, the basic state is chosen at the 300-hPa level over 1979-2010 using the NCEP-NCAR reanalysis data. O'Reilly et al. (2018) reported that results of the barotropic model experiments are insensitive to the basic states chosen from the upper troposphere (e.g., from 350-hPa to 200-hPa). It should

be mentioned that the basic state is chosen from the upper troposphere because the strongest convergence/divergence anomalies generated by the tropical and subtropical SST cooling/warming tend to be observed at the upper troposphere (e.g., Sun et al. 2015; Krishnamurti et al. 2013; O'Reilly et al. 2018; Chen et al. 2020).

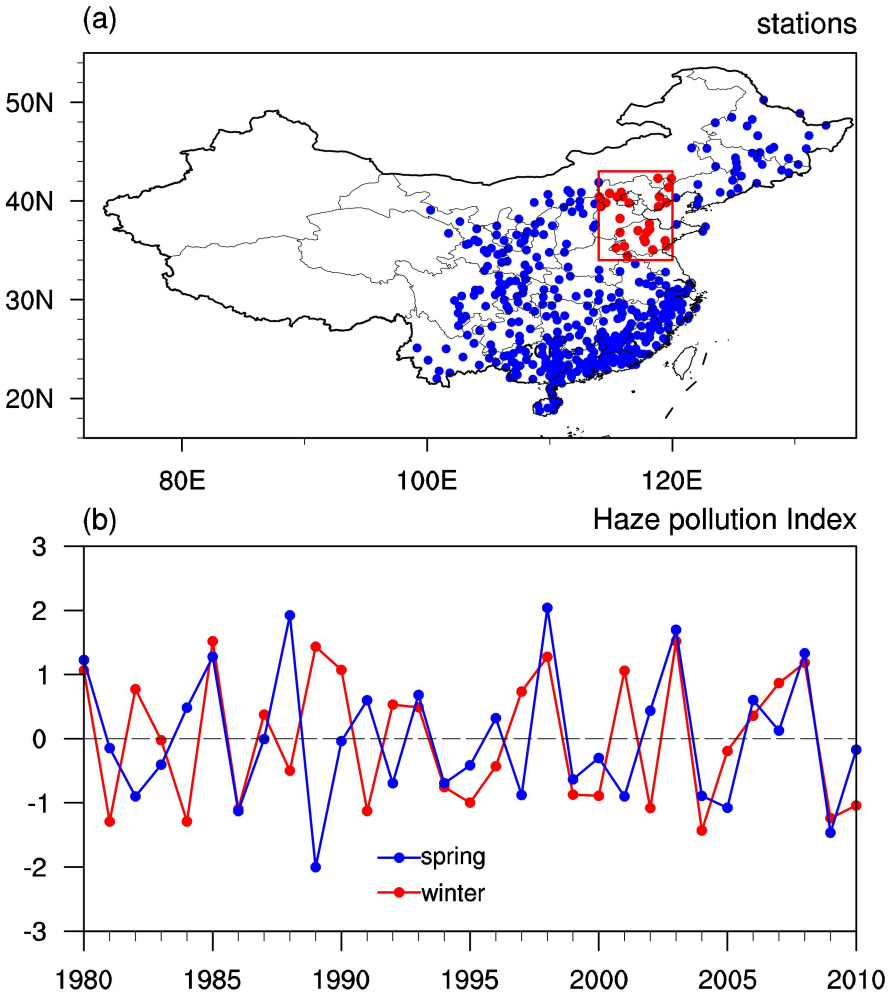

Figure 1. (a) Geographical locations of the meteorological stations (denoted by dots) in China. Red dots represent the meteorological stations in the NCPR. (b) Standardized time series of the NDI in winter (December-January-February-mean, D(0)JF(1) for short) and its following spring (March-April-May-mean, MAM(1) for short) over 1980-2010.

3. Connection of haze pollution over NCPR in winter and spring

Following previous analyses (Yin and Wang 2016; Chen et al. 2019, 2020), the

NCPR corresponds to the region spanning 34°–43°N, 114°–120°E (Fig. 1a). Slight changes of the region to represent NCPR don't affect the main results of this study. Figure 1a shows that there are a total of 28 meteorological observational stations in the NCPR (red dots in the box). As in previous studies (Yin and Wang 2016; Chen et al. 2019, 2020), this analysis defines a NCPR DECC index (NDI for short) by averaging the DECC anomalies over the above 28 stations to describe variation of haze pollution over the NCPR (Fig. 1b). We have examined the first Empirical Orthogonal Function mode (EOF1) of interannual variations of DECC over the NCPR in winter and spring (Figs. 2a and 2b). Spatial patterns of the EOF1 in winter and spring are featured by same-sign DECC anomalies over the NCPR, except for small patch of regions (Figs. 2a and 2b). In addition, the correlation coefficient between the principal component (PC) time series corresponding to the EOF1 of winter DECC anomalies (Fig. 2c, red curve) and the winter NDI (Fig. 1b, red curve) is as high as 0.86, significant at the 99.9% confidence level. Similarly, the correlation coefficient between the PC1 time series of the spring DECC anomalies (Fig. 2c, blue curve) and the spring NDI (Fig. 1b, blue curve) reaches 0.93. Above evidences suggest that the 28 stations in the NCPR can generally be considered as whole.

The correlation coefficient between the winter and spring NDI over 1980–2011 is 0.30, exceeding the 90% confidence level according to the two-tailed Student's *t* test. Note that we have also employed the Monte Carlo method to evaluate the robustness of the winter-spring Haze connection by constructing 10,000 random realizations of spring haze time series. The correlation coefficient with permutation of

90% (95%) confidence is about 0.23 (0.3). Therefore, the Monte Carlo permutation tests demonstrate that the linkage between the winter and spring haze can pass the 95% confidence level. From Fig.1b, 20 out of 32 years with positive or negative winter Haze pollution anomalies are followed by same-sign anomalies of Haze pollution in the following spring over the North China Plain (Fig. 1b). This indicates that the portion is about 62.5% for the persistent relationship between the winter and spring haze. In particular, most of the positive (negative) values of winter NDI are followed by extremely large (small) values of the spring NDI (for example, years in 1980, 1985, 1986, etc.). Above evidences collectively suggest a close in-phase variation of the haze pollution in winter and the following spring. In particular, if haze pollution in winter is less (more) serious over the NCPR, air condition over the NCPR in the following spring also tends to be better (worse) than normal.

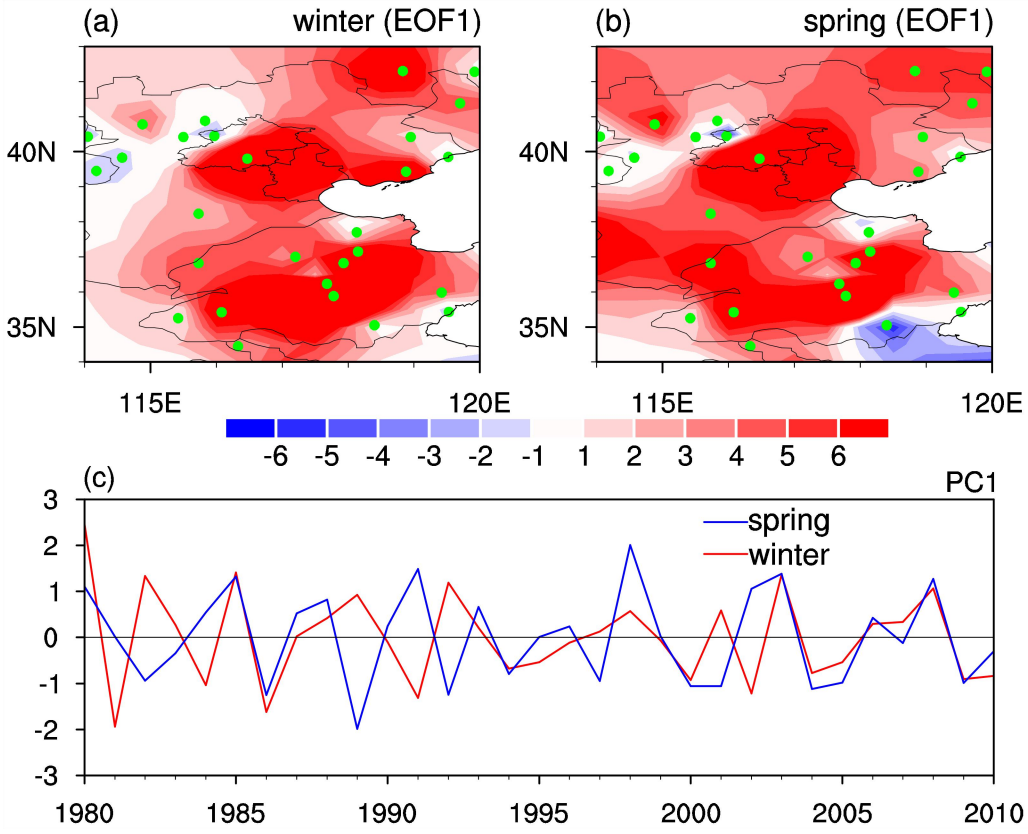

Figure 2. The first EOF mode (EOF1) of interannual anomalies of DECC in (a) winter and (b) spring over the NCPR (i.e. 34°-43°N and 114°-120°E) for the period of 1979-2010. (c) The corresponding PC time series of EOF1 of interannual anomalies of DECC in winter (red curve) and spring (blue curve). The green dots in (a-b) indicate the stations in the NCPR.

Table 1. Lists of the persistent and reverse years.

Persistence (11 years)	Reverse (9 years)
1980, 1985, 1986, 1993, 1994, 1998, 1999, 2003, 2004, 2008, 2009	1982, 1984, 1988, 1989, 1991, 1992, 1997, 2001, 2002

From Fig. 1b, there also exists several years when values of the winter and following spring NDI are strongly opposite, showing out-of-phase variation. In these years, large negative (positive) values of winter NDI are followed by large positive (negative) spring NDI (Fig. 1b). For instance, in 1984 and 1991, the winter NDIs are significantly negative, while the following spring NDIs are significantly positive (Fig. 1b). In 1982 and 1989, large positive values of winter NDI are followed by large negative values of spring NDI (Fig. 1b). In the following, positive (negative) phases of the winter and spring NDIs are identified when the normalized NDIs are larger (less) than 0.43. Previous studies indicated that value of ± 0.43 standard deviation can separate a time series into three portions (positive and negative phases, and normal condition) with nearly the same sample sizes. Note that a use of ± 0.5 standard deviation as the threshold to define anomalous NDI years leads to similar results, but with smaller sample sizes. Table 1 presents the years when winter and spring NDIs are in-phase and out-of-phase. According to Table 1, there are a total of

11 (9) years for the in-phase (out-of-phase). In the following, out-of-phase (in-phase) years are called (reverse) persistent years for convenience of descriptions.

We employ composite analysis to compare evolutions of DECC and atmospheric anomalies between the persistent and reverse years. Note that in performing the composite analysis, we reversed the anomalies when the winter NDI is negative since, to a large extent, the DECC and atmospheric circulation anomalies over the NCPR are symmetric between the positive and negative phases of the winter NDI. Hence, the descriptions below are corresponding to the positive phases of the winter NDI, but also apply to the negative phases except with opposite signs.

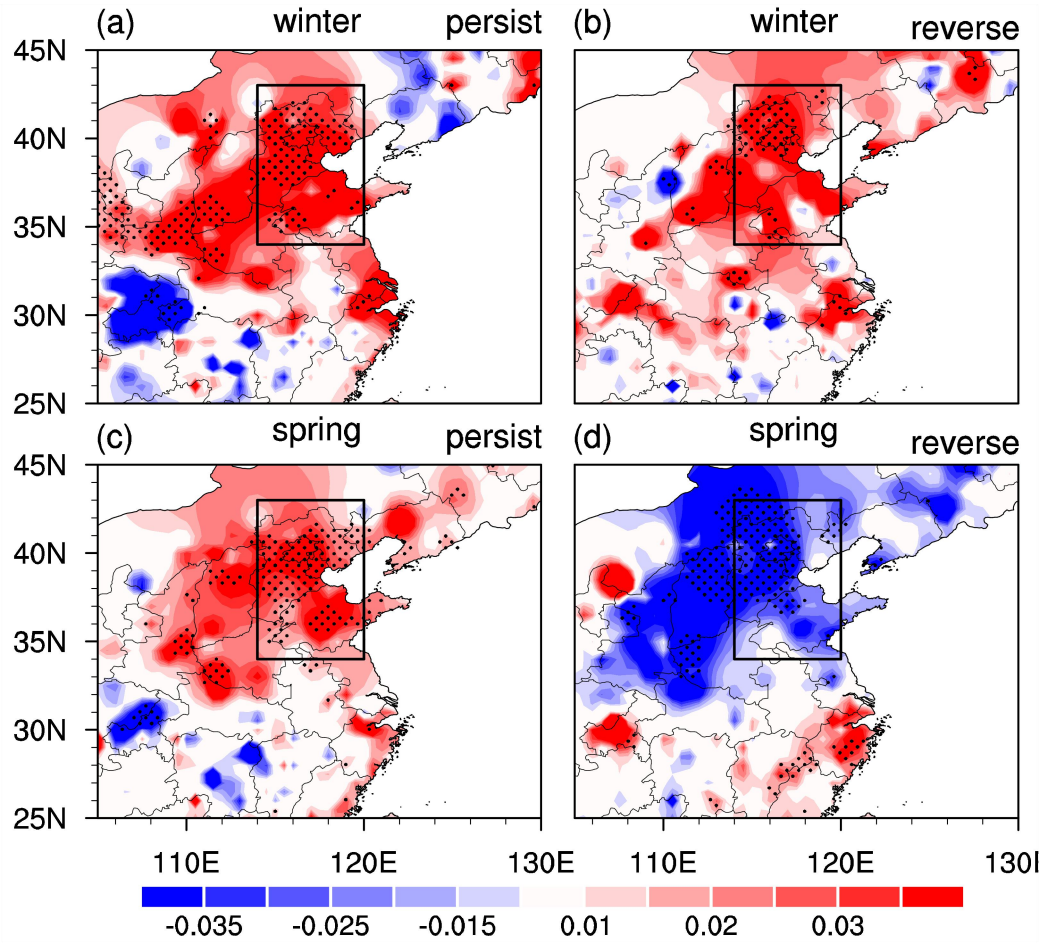

Figure 3. Composite anomalies of DECC (unit: km^{-1}) in (a, b) winter and (c, d) spring in the (left column) persistent years and the (right column) reverse years. Stippling

regions indicate anomalies significant at the 5% level.

Figure 3 shows composite anomalies of DECC in winter and following spring in the persistent and reverse years. For the persistent years, large positive DECC anomalies (indicating more serious haze pollution) are seen over the NCPR and surrounding regions (Fig. 3a). DECC anomalies in winter over southern China are weak, suggesting a weak relation of the haze pollution between northern and southern China, consistent with previous studies (e.g. Li et al. 2017; He et al. 2019). Large positive DECC anomalies over the NCPR are maintained to the succedent spring with comparable amplitude (Figs. 3a and 3c). For the reverse years, large positive DECC anomalies also appear over the NCPR in winter (Fig. 3b). However, in the following spring, the NCPR and surrounding regions are dominated by significantly negative values of DECC (Fig. 3d) (indicating air condition in spring becomes better), which is in sharp contrast to that for the persistent years (Fig. 3c).

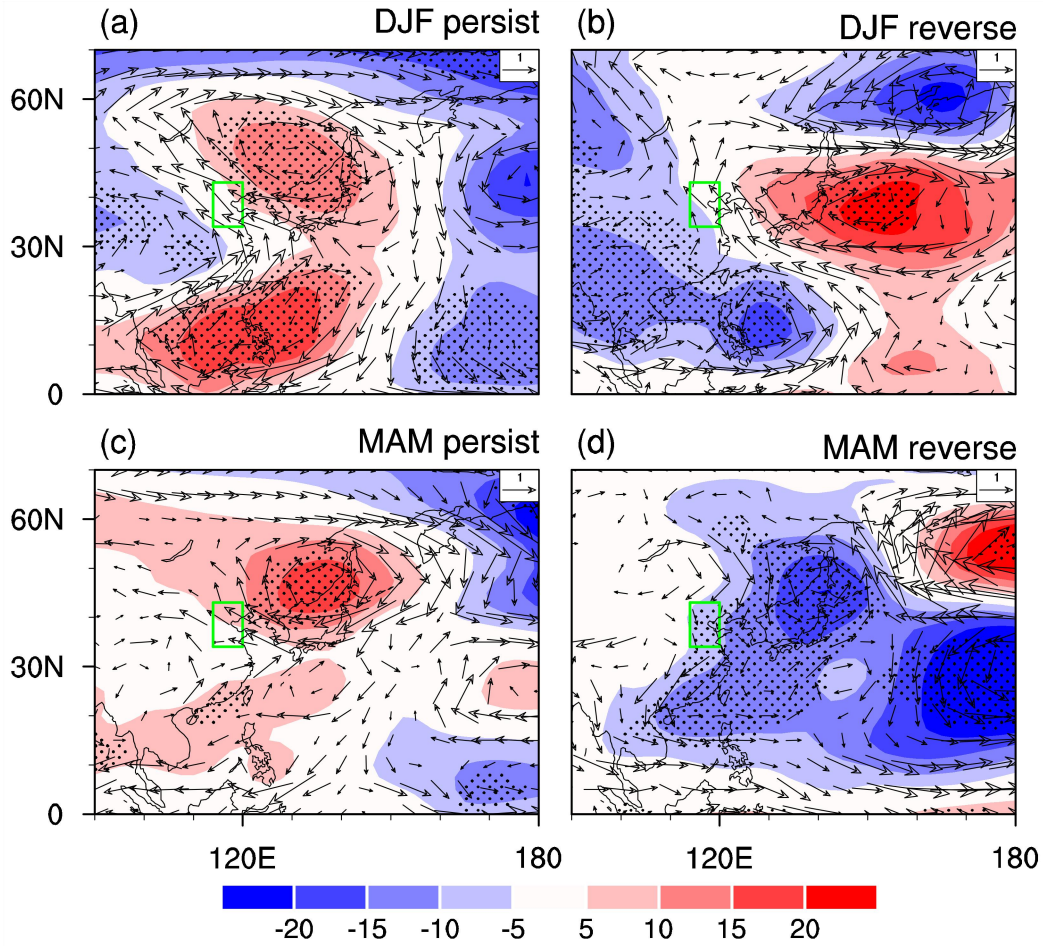

Figure 4. Composite anomalies of 850-hPa winds (vectors, unit: m s^{-1}) and streamfunction (shadings; unit: 10^5 m^2 s^{-1}) in (a, b) winter and (c, d) spring in the (left column) persistent years and the (right column) reverse years. Stippling regions indicate streamfunction anomalies that are statistically significant at the 5% level.

Studies have demonstrated that meteorological conditions related to the atmospheric anomalies can explain above 66% of interannual and interdecadal variations of haze pollution over most parts of Eastern China (Zhang et al. 2014; Chen et al. 2019; He et al. 2019; Dang and Liao 2019; Ma and Zhang 2020). Hence, it is expected that different evolutions of the DECC anomalies from winter to following spring over the NCPR may be associated with the distinct evolutions of atmospheric anomalies. Composite anomalies of winds and streamfunction at 850hPa in winter and following spring for the persistent and reverse years are shown in Fig. 4. In the

persistent years, a significant anticyclonic anomaly is seen over northeast Asia, accompanied by strong southerly wind anomalies over NCPR, and northerly wind anomalies over mid-latitudes North Pacific (Fig. 4a). In addition, another marked anticyclonic anomaly appears over south China sea and Philippine sea, leading to strong southerly wind anomalies over southern China (Fig. 4a). The anomalous anticyclone over northeast Asia and associated southerly wind anomalies over NCPR are maintained to following spring (Fig. 4c).

For the reverse years, a strong anticyclonic anomaly also exists over northeast Asia, but with a southeastward displacement (Fig. 4b) compared to that in the persistent years. Note that NCPR is also dominated by strong southerly wind anomalies (Fig. 4b). In contrast, the south China sea and Philippine sea are covered by an anomalous cyclone, together with northerly wind anomalies over southern China (Fig. 4b). Moreover, an anticyclonic anomaly occurs around the Russian Far East, accompanied by westerly wind anomalies to the north of Japan (Fig. 4b). In the following spring, the pronounced anticyclonic anomaly over northeast Asia and associated southerly wind anomalies over the NCPR are replaced by a marked cyclonic anomaly and northerly wind anomalies (Fig. 4d).

Hence, there appears prominent difference in the atmospheric anomalies over northeast Asia between the persistent and reverse years. Specifically, in the persistent years, the anomalous anticyclone over northeast Asia and southerly wind anomalies over NCPR are maintained from winter to following spring. By contrast, in the reverse years, the wintertime anticyclonic anomaly is replaced by a cyclonic anomaly

over northeast Asia, accompanied by reversal of meridional wind anomalies over NCPR from winter to the succedent spring.

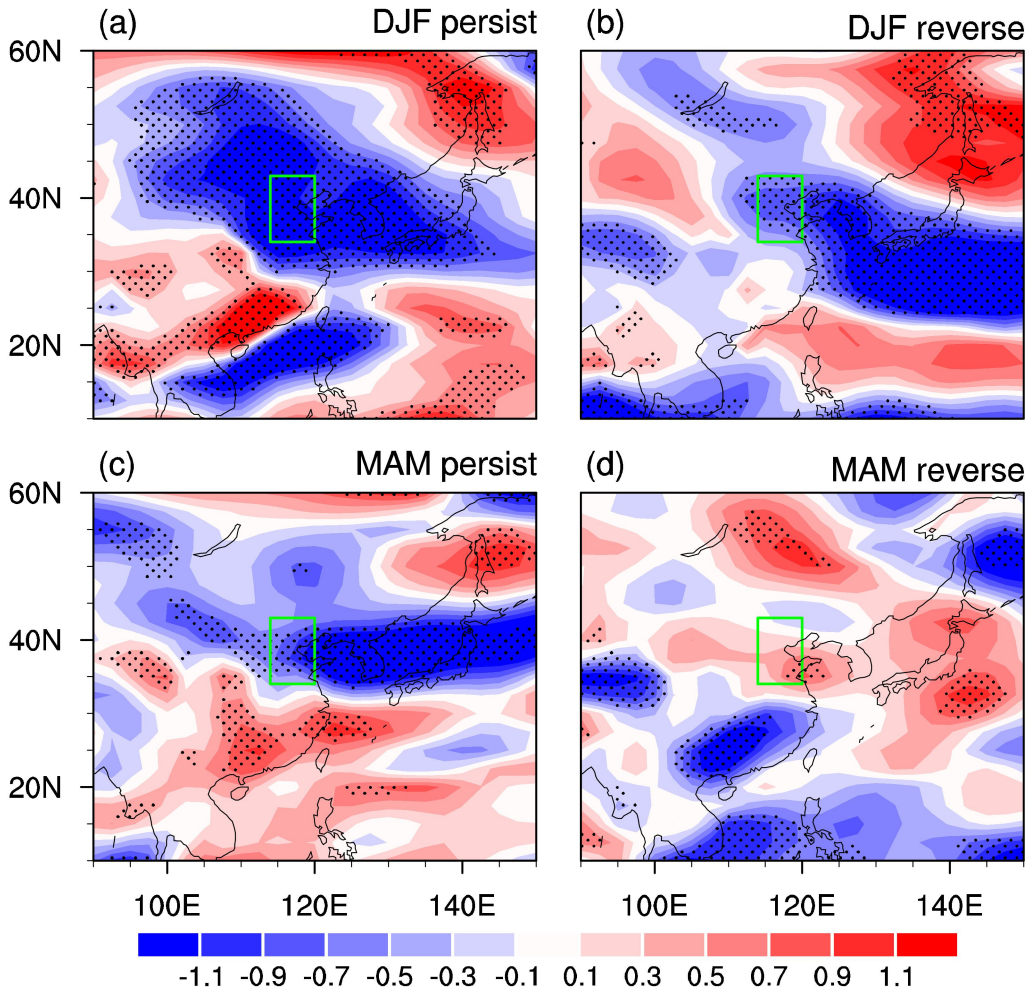

Figure 5. Composite anomalies of 850-hPa wind speed (unit: m s^{-1}) in (a, b) winter and (c, d) spring in the (left column) persistent years and the (right column) reverse years. Stippling regions indicate anomalies that are statistically significant at the 5% level.

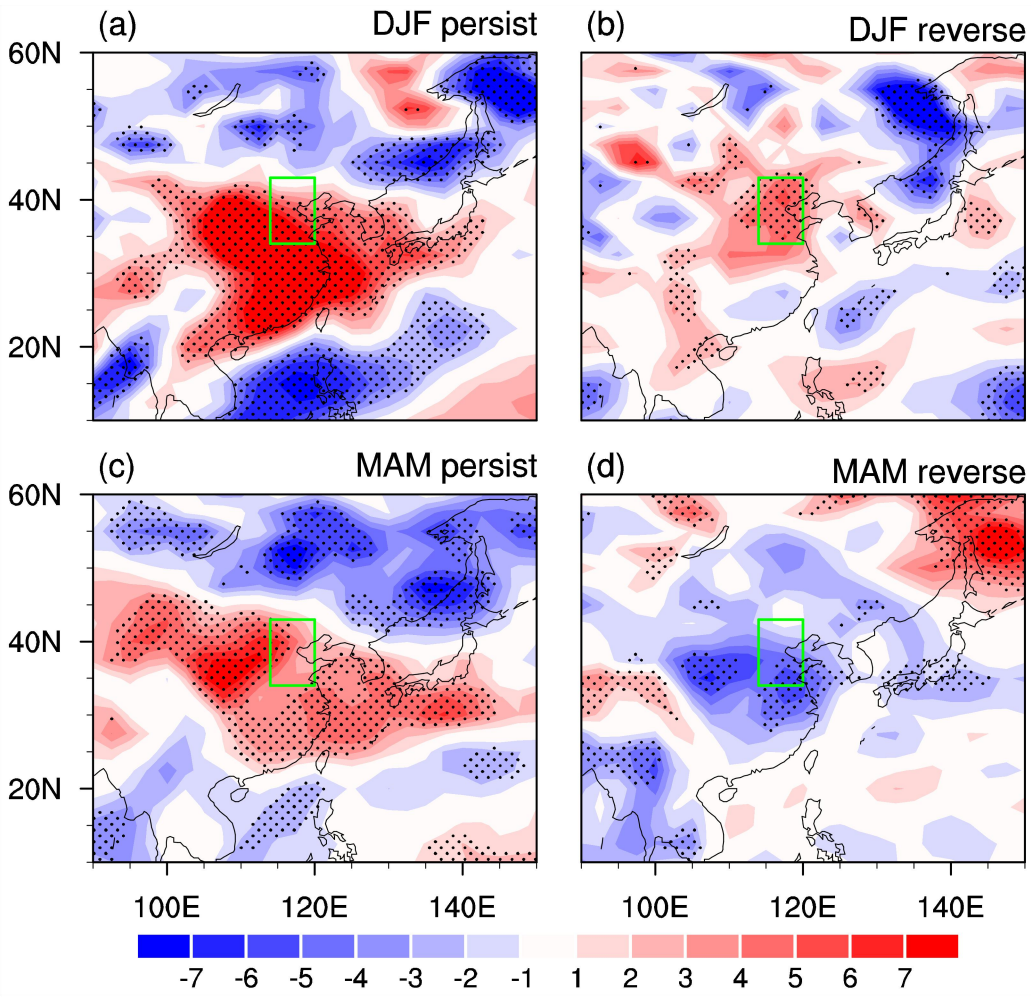

Figure 6. Composite anomalies of 850-hPa relative humidity (unit: %) in (a, b) winter and (c, d) spring in the (left column) persistent years and the (right column) reverse years. Stippling regions indicate anomalies that are statistically significant at the 5% level.

The atmospheric anomalies can impact haze pollution over NCPR in winter and spring via modulating surface wind speed, relative humidity and boundary layer height (BLH) (e.g. Hang et al. 2013; Chen et al. 2019, 2020; He et al. 2019; Dang and Liao 2019; Li et al. 2020). The increase (decrease) in the surface wind speed is (not) conducive to horizontal diffusion of pollutants, thus contributing to below (above) normal DECC and less (more) serious haze pollution (Chen et al. 2019; Li et al. 2020). Increase (decrease) in the BLH tends to favor (suppress) vertical diffusion of pollutant,

and thus results in below (above) normal DECC (Zhang et al. 2016; Wang et al. 2018). Furthermore, large (small) relative humidity is (not) conducive to the generation of secondary organic compounds and secondary aerosol species (such as SO_4^{2-} and NO_3^-), which contribute to more (less) serious haze pollution over NCPR (Yu et al. 2005; Hennigan et al. 2008; Chen et al. 2019; Li et al. 2020; Ma and Zhang 2020).

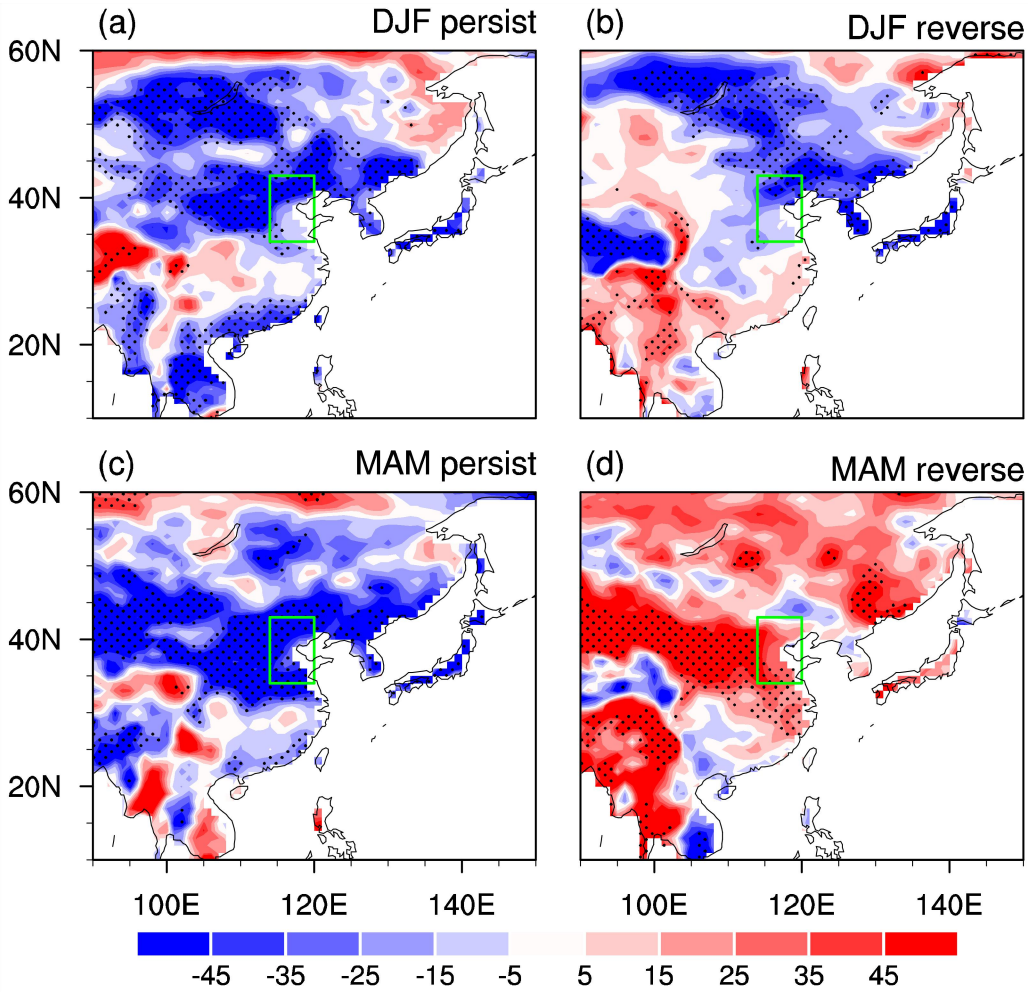

Figure 7. Composite anomalies of boundary layer height (BLH, unit: m) in (a, b) winter and (c, d) spring in the (left column) persistent years and the (right column) reverse years. Stippling regions indicate anomalies that are statistically significant at the 5% level.

Composite anomalies of low-level (850-hPa) wind speed, relative humidity and BLH in winter and spring are shown in Figs.5-7, respectively. In winter, low-level

wind speed is significantly decreased over the NCPR with a northwestward extension to the Lake Baikal and an eastward extension to western North Pacific for both the persistent and reverse years (Figs. 5a and 5b). The southerly wind anomalies to the western side of the anticyclonic anomaly over northeast Asia (Figs. 4a and 4b) as opposite to the climatological northerly winds dominated by East Asian winter monsoon (not shown), and lead to decreases in the total wind speed (Figs. 5a and 5b), which contributes to more serious haze pollution (Figs. 3a and 3b). In addition, southerly winds anomalies tend to bring more water vapor northward from Southern Ocean and result in an increase in the relative humidity (Figs. 6a and 6b), which are conducive to formation of secondary aerosol species (Yu et al. 2005; Hennigan et al. 2008; Chen et al. 2019) and contribute to more serious haze pollution over NCPR in winter (Figs. 2a and 2b). Moreover, large decrease in the BLH over the NCPR, which is associated with the anomalous anticyclone there, also contributes to above normal DECC via suppressing the vertical diffusion of pollutant (Figs. 7a and 7b) (Zhang et al. 2016; Wang et al. 2018). In the persistent years, sustenance of the anticyclonic anomaly over northeast Asia and southerly wind anomalies over NCPR to the following spring (Fig. 4c) contributes to above normal DECC in spring (Fig. 3c) via reducing surface wind speed and BLH (Figs. 5c and 7c), and increasing relative humidity (Fig. 6c). By contrast, in the reverse years, reversal of atmospheric anomalies over northeast Asia from anticyclonic anomaly in winter (Fig. 4b) to cyclonic anomaly in the following spring (Fig. 4d) results in the inverted DECC anomalies over NCPR (Figs. 3b and 3d). In spring, the cyclonic anomaly over

406 northeast Asia increase the low-level total wind speed (Fig. 5d) and BLH (Fig. 7d),
407 which are conducive to the horizontal and vertical dispersion of pollutants and
408 contribute to a better air condition. Additionally, the anomalous northerly winds (Fig.
409 4d) lead to decrease in the relative humidity (Fig. 6d) via carrying colder and drier air
410 from higher latitude, suppressing generation of secondary organic compounds and
411 secondary aerosol species, and also contributing to mitigation of haze pollution (Fig.
412 3d). Above evidences suggest that the distinct evolutions of haze pollution over
413 NCPR between the persistent and reverse years are closely related to the different
414 evolutions of atmospheric anomalies over northeast Asia.

415 Atmospheric anomalies over northeast Asia related to interannual variations of
416 haze pollution over NCPR are closely associated with upstream atmospheric wave
417 train over North Atlantic and mid-high latitudes Eurasia. Studies have demonstrated
418 that atmospheric wave trains originated from North Atlantic across Eurasia to East
419 Asia have a strong contribution to interannual variations of haze pollution and climate
420 anomalies over North China (Yin and Wang 2016, 2017; Zhao et al. 2019; Chen et al.
421 2019, 2020). Composite anomalies of geopotential height at 500-hPa over larger areas
422 in winter and succedent spring for the persistent and reverse years are presented in Fig.
423 8. To examine the possible sources of the atmospheric wave trains over Eurasia, we
424 also present the wave activity fluxes in Fig. 8, which describe propagation directions
425 of the atmospheric Rossby waves. Spatial structures of the geopotential height
426 anomalies at 850-hPa and 200-hPa (not shown) are highly similar to those at 500-hPa
427 in Fig. 8, indicating a vertically barotropic structure of the atmospheric anomalies

over mid-high latitudes of North Atlantic and Eurasia.

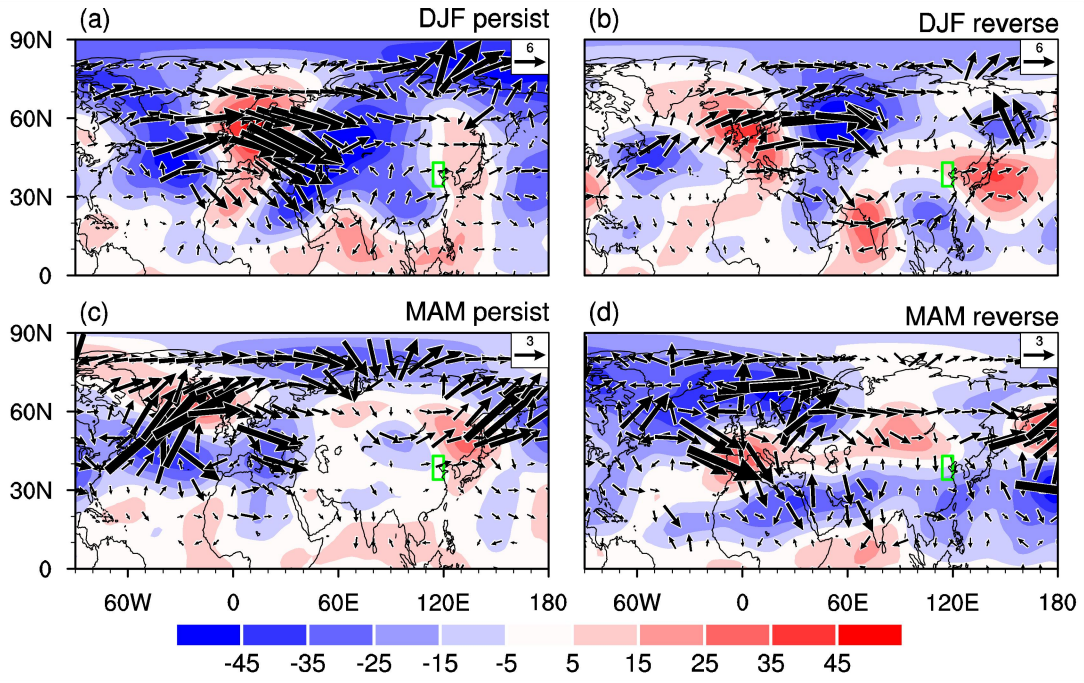

Figure 8. Composite anomalies of 500-hPa geopotential height (shadings, unit: m) and wave activity fluxes (vectors; unit: m^2 s^{-2}) in (a, b) winter and (c, d) spring in the (left column) persistent years and the (right column) reverse years.

In the persistent years, an EAWR-like teleconnection pattern is obviously observed extending from North Atlantic across Europe to East Asia, with negative geopotential height anomalies (corresponding to cyclonic anomalies) over mid-high latitudes North Atlantic and central Eurasia, and positive geopotential height anomalies (corresponding to anticyclonic anomalies) over west Europe and northeast Asia (Fig. 8a). The pattern correlation coefficient between the EAWR-related 500-hPa geopotential height anomalies and those in Fig. 8a over the North Atlantic and Eurasian regions (i.e. 20°–90°N and 70°W–130°E) reaches 0.65, significant at the 99.9% confidence level. Hence, in the persistent years, the EAWR teleconnection contributes largely to the formation of the anticyclonic anomaly over northeast Asia in

443 winter. In the reverse years, spatial structure of the 500-hPa geopotential height
444 anomalies over mid-high latitudes of North Atlantic and Eurasia (Fig. 8b) bears a
445 close resemblance to that for the persistent years (Fig. 8a), and also resembles the
446 EAWR teleconnection pattern. We have also calculated the pattern correlation
447 coefficient between the 500-hPa geopotential height anomalies in Fig. 8b and those
448 related to the winter EAWR over the same region of 20°–90°N and 70°W–130°E. The
449 pattern correlation coefficient is as high as 0.85, slightly higher than that in the
450 persistent years (r=0.65), suggesting that the EAWR teleconnection pattern also has a
451 strong contribution to the formation of the wintertime anticyclonic anomaly over
452 Northeast Asia and haze pollution over the NCPR in the reverse years. Above results
453 are consistent with Yin and Wang (2017) and Chen et al. (2020). Yin and Wang (2017)
454 demonstrated that the EAWR teleconnection is the most important atmospheric wave
455 train modulating haze pollution over North China. Chen et al. (2020) reported that the
456 winter EAWR teleconnection has a stable and strong impact on the interannual
457 variation of haze pollution over the NCPR via calculating the running correlation
458 coefficients between the winter EAWR index and NDI. Note that there exist several
459 differences in the spatial structure of the wintertime EAWR teleconnection between
460 the persistent and reverse years (Figs. 8a and 8b). In particular, the center of negative
461 geopotential height anomalies over central Eurasia in the persistent years (Fig. 8a) is
462 stronger and shifts southward compared to that in the revere years (Fig. 8b). In
463 addition, negative geopotential height anomalies over western North Atlantic extend
464 more southwestward for the revere years (Figs. 8a and 8b). Differences in the spatial

structure of the winter EAWR between the persistent and reverse years may be partly due to differences in the background mean circulation (Chen and Wu 2017; Wang et al. 2019). Detailed investigation of the factors for the changes of the spatial pattern of the winter EAWR is out of the scope of this study. Furthermore, it is interesting to note that an atmospheric Rossby wave exists over subtropical region propagating along the subtropical Jet stream to extend from north Africa across south Asia and then turn northeastward to northeast Asia in the reverse years (Fig. 8b). This subtropical wave train also has a contribution to the formation of the anticyclonic anomaly over Northeast Asia and interannual variation of haze pollution over the NCPR as has been indicated by Chen et al. (2020).

In spring, a negative NAO-like pattern appears over North Atlantic in the persistent years, featured by negative geopotential height anomalies around 40°-50°N and positive anomalies over 60°-70°N in the persistent years (Fig. 8c). The pattern correlation coefficient between the spring NAO-related 500-hPa geopotential height anomalies and the composted 500-hPa geopotential height anomalies in Fig. 6c over North Atlantic region (30°–80°N and 20°W–60°W) is as high as -0.75. This result is consistent with Chen et al. (2019), which indicated that negative (positive) phase of the spring NAO contributes to formation of an anomalous anticyclone (cyclone) over Northeast Asia and leads to more (less) serious haze pollution over NCPR via eastward propagating wave train. However, in the reverse years, there exists a positive NAO-like pattern over the North Atlantic (Fig. 8d), which is in sharp contrast to that in the persistent years (Fig. 8c). In particular, the pattern correlation between the

500-hPa geopotential height anomalies in Fig. 8c and spring NAO-related anomalies over 30°–80°N and 20°W–60°W reaches 0.6. As indicated by Chen et al. (2019), the spring positive NAO would contribute to below-normal DECC over the NCPR.

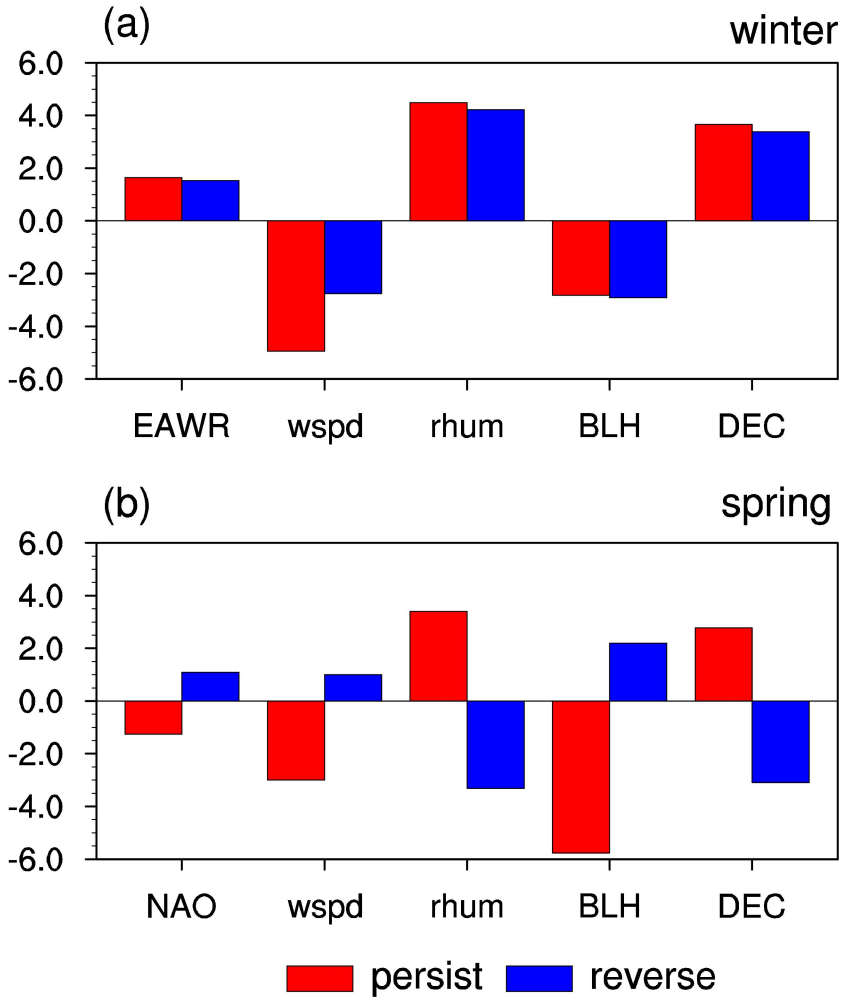

Figure 9. (a) Composite anomalies of the EAWR index, wind speed at 850-hPa (4^{-1} m s^{-1}), relative humidity at 850-hPa (%), BLH (10^{1} m), and DECC (10^{-2} km^{-1}) averaged over NCPR in winter for the persistent years (red bars) and the reverse years (blue bars). (b) Composite anomalies of the NAO index, wind speed at 850-hPa (m s^{-1}), relative humidity at 850-hPa (%), BLH (10^{1} m), and DECC (km^{-1}) averaged over NCPR in spring for the persistent years (red bars) and the reverse years (blue bars).

The distinct evolutions of NCPR-average DECC, surface wind speed, relative humidity, the winter EAWR index, and spring NAO index are summarized in Fig. 9. In winter, positive phase of the EAWR teleconnection contributes to anticyclonic

anomalies over northeast Asia and associated southerly wind anomalies over the NCPR, which further lead to positive DECC anomalies both in the persistent and reverse years via reducing surface wind speed and BLH, and increasing relative humidity (Fig. 9a). In spring, negative (positive) phase of the spring NAO contributes to formation of the anomalous anticyclone (cyclone) over northeast Asia, and results in positive (negative) DECC anomalies over the NCPR via increasing (decreasing) the relative humidity and decreasing (increasing) the surface wind speed and BLH in the persistent (reverse) years (Fig. 9b). Above evidences strongly indicate that different evolutions of atmospheric anomalies over North Atlantic and mid-high latitude Eurasia play a crucial role in the distinct evolutions of the haze pollution over NCPR.

4. Mechanism for the different evolutions of atmospheric anomalies over North Atlantic and Eurasia

What is the possible mechanism for the different evolutions of atmospheric anomalies over North Atlantic and Eurasia? Considering that the internal atmospheric process could not explain the connection of the atmospheric anomalies between two seasons, the evolution of atmospheric anomalies over North Atlantic may be related to the underlying SSTA. Previous studies have demonstrated that North Atlantic is the region with strong air-sea interaction (Czaja et al. 2002; Czaja and Frankignoul 2002; Huang and Shukla 2005; Pan 2005; Peng et al. 2003; Wu et al. 2009; Chen et al. 2016, 2018). On one hand, atmospheric anomalies over North Atlantic could lead to SSTA via modulating surface heat fluxes (Czaja et al. 2002; Huang and Shukla 2005; Wu et

522 al. 2009; Chen et al. 2015). The connection between the atmospheric anomalies and
523 SSTA over North Atlantic is the closest when atmospheric anomalies lead SSTA by
524 about one month (Czaja and Frankignoul 2002; Huang and Shukla 2005). On the
525 other hand, SSTA in the North Atlantic have a strong feedback on the overlying
526 atmospheric circulation via the heating-induced atmospheric Rossby wave response
527 and the interaction between low frequency mean flow and synoptic-scale eddy (Peng
528 et al. 2003; Pan 2005; Czaja and Frankignoul 2002; Chen et al. 2020). In particular, a
529 number of studies have suggested that the development and evolution of atmospheric
530 anomalies and SSTA over North Atlantic are attributed to the positive air-sea
531 interaction process there (Czaja and Frankignoul 1999; Rodwell and Folland 2002;
532 Visbeck et al. 2003; Czaja et al. 2003; Wu and Liu 2005; Hu and Huang 2006; Chen
533 et al. 2019; Chen et al. 2020).

534 Evolutions of SSTA in the North Atlantic are examined in Fig. 10. In the
535 persistent years, significant cold SSTA are seen in the central North Atlantic around
536 30^{o}N and off the east coast of Canada, together with notable warm SSTA in
537 subtropical eastern North Atlantic with a northeastward extension to the west coast of
538 Europe (Fig. 10a). The warm SSTA in the subtropical northeastern Pacific and the
539 cold SSTA in the central North Atlantic are maintained to the following spring with an
540 increase in the amplitude. In addition, high latitude North Atlantic is covered by warm
541 SSTA in spring. This forms a significant tripolar SSTA pattern in spring. Note that the
542 tripolar SSTA pattern is also the first EOF mode of interannual variation of SSTA in
543 the North Atlantic (not shown) (Chen et al. 2016, 2020). Studies have demonstrated

that warm (cold) SSTA in the tropical and subtropical North Atlantic related to the tripolar SST anomaly pattern could induce a negative NAO-like pattern via the Rossby wave type atmospheric response and wave-mean flow interaction process according to the observational analysis and numerical experiments (Peng et al. 2003; Pan 2005; Czaja and Frankignoul 2002; Chen et al. 2016, 2020).

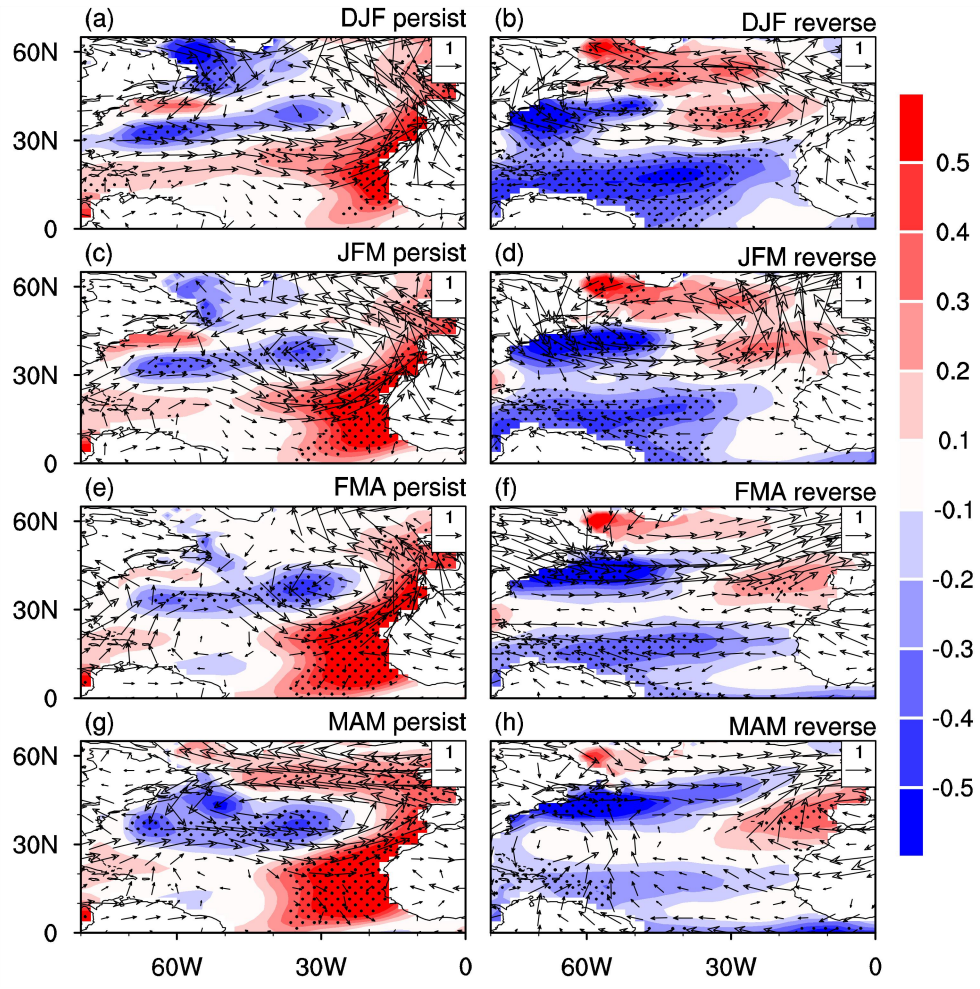

Figure 10. Composite anomalies of SST (°C) and 850-hPa winds (m s^{-1}) in (a, b) D(0)JF(1), (c, d) JFM(1), (e, f) FMA(1), and (g, h) MAM(1) for (left column) the persistent years and (right column) the reverse years. Stippling regions in the figure indicate SST anomalies that are statistically significant at the 5% level.

In the reverse years, significant cold SSTA are seen in the tropical and subtropical western North Atlantic in winter (Fig. 10b), which can maintain to

following spring with a decrease in the amplitude (Figs. 10h), which are in sharp contrast to those in the persistent years (Figs. 10a, c, e, and g). It is reasonable to speculate that the opposite SSTA in the tropical and subtropical North Atlantic may be responsible for the opposite atmospheric anomalies over North Atlantic, which will be confirmed later based on the linear barotropic model.

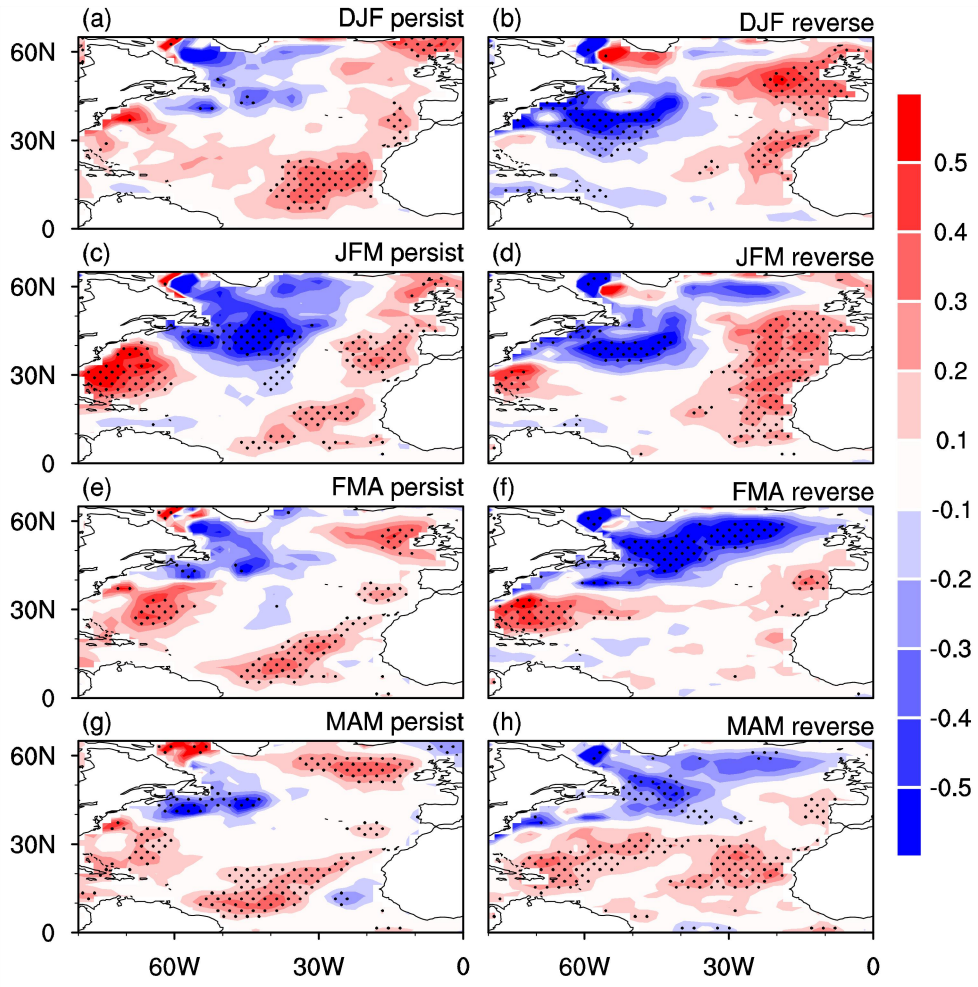

Figure 11. Composite anomalies of surface net heat fluxes (W m^{-2}) in (a, b) D(0)JF(1), (c, d) JFM(1), (e, f) FMA(1), and (g, h) MAM(1) for (left column) the persistent years and (right column) the reverse years. Stippling regions in the figure indicate anomalies that are statistically significant at the 5% level.

Evolutions of SSTA in the North Atlantic from winter to the following spring are related to the air-sea interaction. Figure 11 shows composite anomalies of the surface

net heat fluxes for the persistent and reverse years. Values of the surface heat fluxes have been taken to be positive (negative) when their directions are downward (upward), which contribute to warm (cold) SSTA. We have also examined composite anomalies of SST tendency (not shown). It shows that spatial patterns of anomalies of SST tendency in most parts of North Atlantic are similar to those of the surface net heat fluxes anomalies. This suggests that changes in the surface net heat fluxes can largely explain evolutions of SSTA in the North Atlantic from winter to the following spring. For example, in the persistent years, significant positive net heat flux anomalies are seen over the subtropical northeastern Atlantic from winter to spring (Figs. 11a, 11c, 11e, and 11g), which could explain the formation and enhancement of the positive SSTA there (Figs. 11a, 11c, 11e, and 11g). In addition, the negative surface net heat flux anomalies to the east of the Canada explain generation and maintenance of the negative SSTA there. Moreover, the positive surface net heat flux anomalies over high latitudes contribute to warm SSTA. In the reverse years, positive net heat flux anomalies appear off the west coast of west Europe (Figs. 11b, d, f, h), which explain maintenance of the warm SSTA (Figs. 10b, d, f, h). In addition, positive net surface heat flux anomalies over subtropical western North Atlantic in FMA and MAM (Figs. 11f and 11h) explain the decrease in the amplitude of the negative SSTA there (Figs. 10f and 10h).

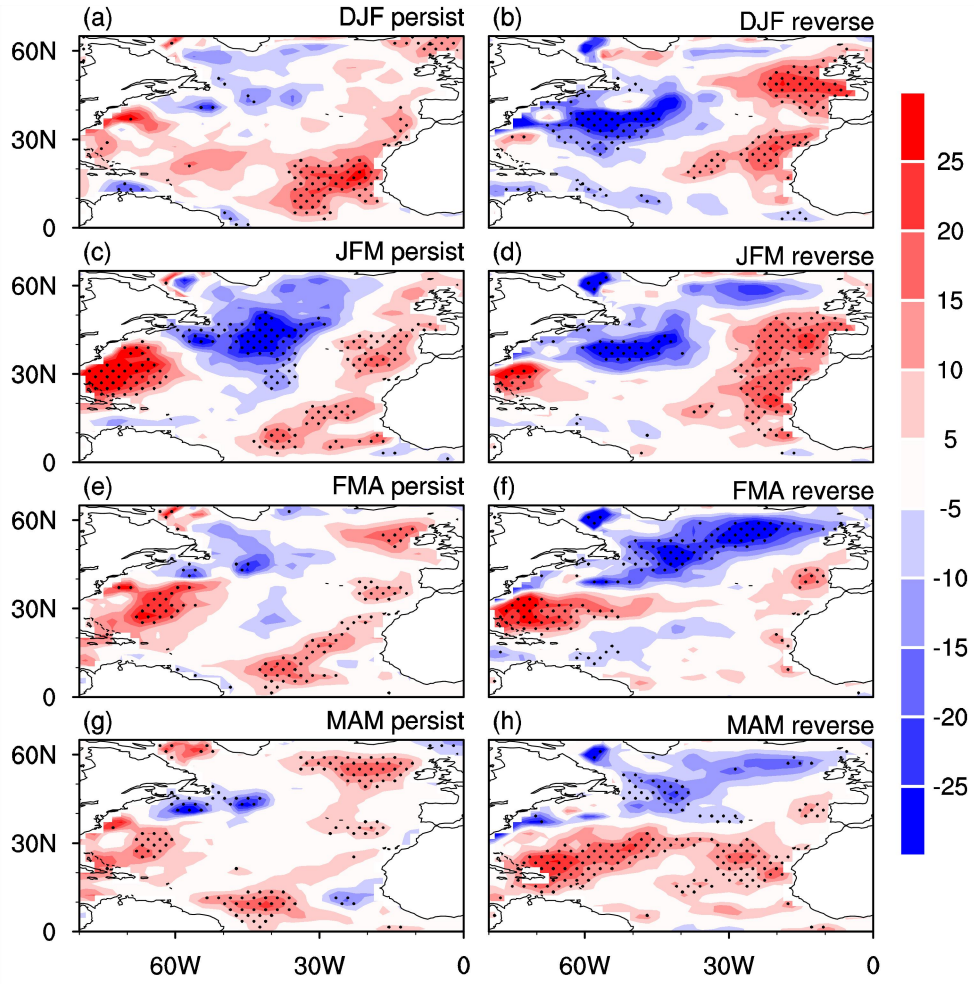

587

588 **Figure 12.** Composite anomalies of surface latent heat fluxes (W m^{-2}) in (a, b)
589 D(0)JF(1), (c, d) JFM(1), (e, f) FMA(1), and (g, h) MAM(1) for (left column) the
590 persistent years and (right column) the reverse years. Stippling regions in the figure
591 indicate anomalies that are statistically significant at the 5% level.

592 Surface net heat flux anomalies are related to the overlying atmospheric
593 circulation changes. Surface heat flux consists of four components, including the
594 surface longwave and shortwave radiations, and surface latent and sensible heat fluxes.
595 We find that surface net heat flux anomalies (Fig. 12) are dominated by changes in the
596 surface latent heat flux (Fig. 12). Amplitudes of the surface sensible heat fluxes, and
597 surface longwave and shortwave radiations are much weaker compared to that of the
598 surface latent heat flux, and thus are not presented. In the persistent years, the

599 anomalous southwesterly winds over subtropical northeastern Atlantic in winter and
600 spring oppose the climatological northeasterly winds (Figs. 10a and 10g). This results
601 in decrease in the total wind speed and decrease in the upward latent heat flux (Figs.
602 12a and 12g) and thus contribute to warm SSTA (Figs. 10a and 10g). Note that the
603 warm SSTA in the subtropical northeastern Atlantic could induce an anomalous
604 cyclone to its northwestward direction via Rossby wave type atmospheric response
605 (Czaja and Frankignoul 1999, 2002; Huang and Shukla 2005; Hu and Huang 2006;
606 Chen et al. 2016, 2020) and help maintain the anomalous cyclone over mid-latitude
607 North Atlantic from winter to spring (Figs. 10a and 10g). Similarly, the anomalous
608 easterly winds along 60°N over North Atlantic oppose the climatological westerly
609 winds (Figs. 10a and 10g), which lead to warm SSTA there via reduction of wind
610 speed and upward latent heat fluxes (Figs. 12a and 12g). By contrast, the anomalous
611 northerly winds to the western flank of the cyclonic anomaly bring colder and drier air
612 from higher latitude (Figs. 10a and 10g), which increase the upward latent heat flux
613 and contribute to cold SSTA (Figs. 12a and 12g). In the reverse years, southerly wind
614 anomalies off the west coast of west Europe carry warmer and wetter air northward
615 from lower latitudes and lead to warm SSTA (Figs. 10b and 10h) via reduction of
616 upward latent heat flux (Figs. 12b and 12h). In winter, northerly wind anomalies over
617 the subtropical western North Atlantic increase the trade wind (Fig. 10b), which result
618 in enhancement of surface latent heat flux (Fig. 12b) and partly contribute to cold
619 SSTA (Fig. 10b). The above analyses suggest that evolution of SSTA in the North
620 Atlantic from winter to subsequent spring is closely related to the air-sea interaction

621 over the North Atlantic.

622 The notable differences in the SSTA in the tropical and subtropical North
623 Atlantic may explain the different atmospheric anomalies over North Atlantic and
624 Eurasia between the persistent and reverse years, with negative (positive) spring
625 NAO-like pattern and anticyclonic (cyclonic) anomaly over northeast Asia in the
626 persistent (reverse) years. Studies have demonstrated that springtime SSTA in the
627 tropical and subtropical North Atlantic have a strong impact on the atmospheric
628 circulation and associated climate anomalies over North Atlantic and Eurasia (Wu et
629 al. 2009; Wu et al. 2011; Chen et al. 2016, 2020). In particular, SSTA in the tropical
630 and subtropical regions could induce strong vertical motion and atmospheric heating
631 anomalies reaching to the upper-level troposphere (Ting 1996; Wu et al. 2009;
632 Hodson et al. 2010; Wu et al. 2011; Sun et al. 2015; Chen et al. 2020). Then, the
633 divergent/convergent anomalies at the upper-level troposphere induced by the SSTA
634 could be considered as effective sources for the generation of the atmospheric Rossby
635 wave (Watanabe 2004; Chen and Huang 2012; Zuo et al. 2013; Chen et al. 2020).
636 Considering that the atmospheric wave trains extending from the North Atlantic to the
637 Eurasia in Figs. 6c and 6d resemble an atmospheric stationary Rossby wave with an
638 equivalent barotropic vertical structure, the mechanism for their formation could be
639 examined based on the barotropic vorticity equation (Wu et al. 2011; Zuo et al. 2013;
640 Chen et al. 2016, 2020; O'Reilly et al. 2018). Hence, in the following, we perform
641 model simulations with barotropic model (Sardeshmukh and Hoskins 1988; Watanabe
642 2004; O'Reilly et al. 2018) to confirm the possible roles of the spring SSTA in the

643 North Atlantic in the formation of atmospheric anomalies over the North Atlantic and
644 Eurasia. Studies indicate that the barotropic model has a good performance in
645 capturing the key dynamics of the atmospheric response to the atmospheric heating
646 associated with the SSTA in the tropical and subtropical regions (Wu et al. 2011; Sun
647 et al. 2015; Zuo et al. 2013; Chen et al. 2016, 2020). Three experiments are performed:
648 the first experiment forced by the spring climatological mean vorticity (denoted as
649 EXP_Ctrl); the second experiment forced by the spring climatological mean vorticity
650 plus the given divergent anomalies over the subtropical northeastern Atlantic with a
651 center at 20°N, 20°W and maximum intensity of $7\times10^{-6}\times s^{-1}$ according to the spatial
652 pattern of spring SSTA in Fig. 10g (denoted as EXP_persist); the third experiment
653 forced by the spring climatological mean vorticity plus the given convergent
654 anomalies over the subtropical northwestern Atlantic with a center at 15°N, 60°W and
655 maximum intensity of $7\times10^{-6}\times s^{-1}$ according to the spatial pattern of spring cold
656 SSTA in tropical North Atlantic in Fig. 10h (denoted as EXP_reverse). Above three
657 experiments are integrated for 40 days.

658 Figure 13a displays difference of atmospheric responses averaged during model
659 days 31-40 between EXP_persist and EXP_Ctrl with green contours representing the
660 prescribed divergent anomalies. In addition, difference of the responses between
661 EXP_reverse and EXP_Ctrl is exhibited in Fig. 13b. It is noted that the barotropic
662 model experiments can reach equilibrium state quickly with only several days
663 (Sardeshmukh and Hoskins 1988; Zuo et al. 2013; Chen et al. 2016). Hence, the
664 atmospheric responses averaged during model days 31-40 are highly similar to those

averaged during other model days (not shown) (e.g. 25-35 days and 20-40 days). In generally, the barotropic model experiments can well reproduce the distinct atmospheric anomalies between the persistent and reverse years.

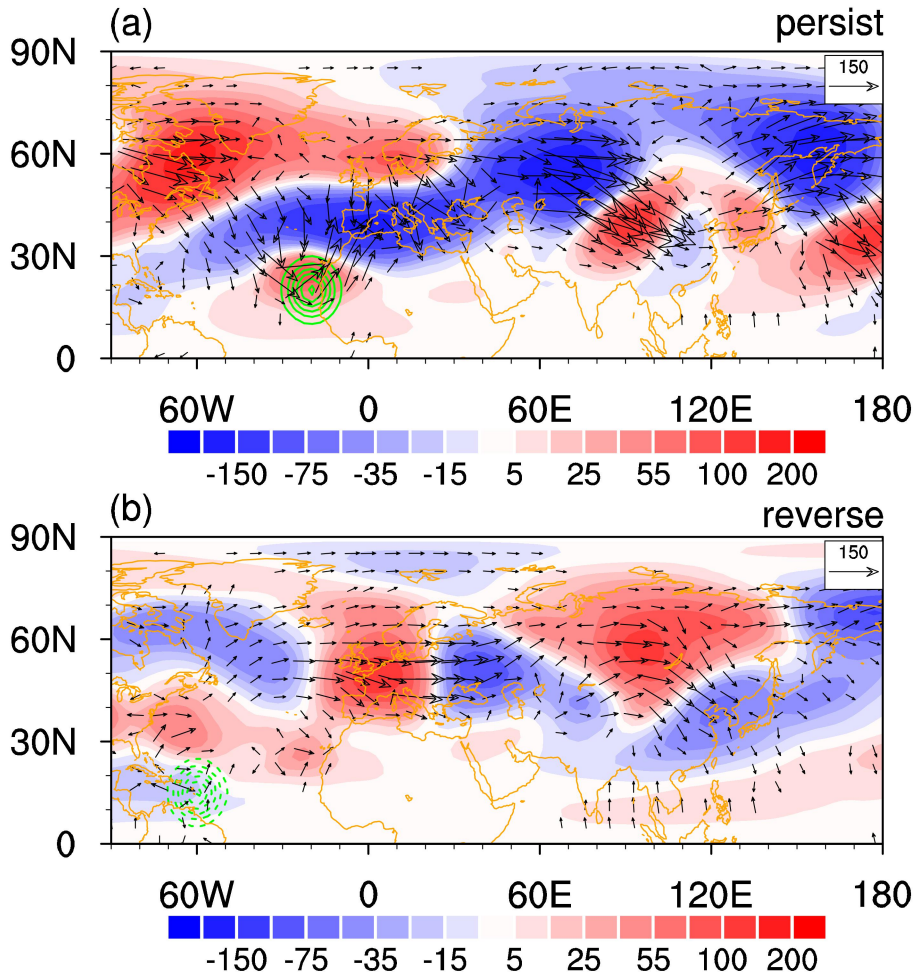

Figure 13. (a) Barotropic model height perturbation (unit: m) averaged from days 31 to 40 as a response to the given divergence anomaly (green contours with an interval of 10^{-6} s^{-1}) over the subtropical eastern North Atlantic with the center at 20°N, 20°W. (b) Barotropic model height perturbation (unit: m) averaged from days 31 to 40 as a response to the given convergence anomaly (green contours with an interval of 10^{-6} s^{-1}) over the subtropical western North Atlantic with the center at 15°N, 60°W. Vectors in (a)-(b) indicate the corresponding wave activity fluxes.

In response to the prescribed divergent anomalies over the subtropical northeastern Atlantic related to the warm SSTA there, there appears a positive

NAO-like pattern with negative geopotential anomalies over mid-latitudes (along 30°N) and positive anomalies over high-latitudes (along 60°N) North Atlantic (Fig.13a), largely similar to the spatial pattern of spring atmospheric anomalies in the persistent years in Fig. 8c. By contrast, in response to the prescribed convergent anomalies over the subtropical northwestern Atlantic associated with the cold SSTA, there exists a negative NAO-like pattern, with negative geopotential anomalies over high-latitudes (along 60°N) and negative anomalies over mid-latitudes (along 30°N) North Atlantic (Fig.13b), in concert with the spatial distribution of the atmospheric anomalies in the reverse years in Fig. 8d. In addition, it is surprising to see that the barotropic model experiment well simulate the anticyclonic (cyclone) anomaly over northeast Asia and related southerly (northerly) wind anomalies over the NCPR in response to the prescribed forcing in the subtropical northeastern (northwestern) Atlantic as indicated in Fig. 13a (13b). This is consistent with the observed spring atmospheric anomalies over East Asia for the persistent (reverse) years, although the centers of the wave train over Eurasia in the barotropic experiments are not totally identical to those in the observations. In general, the above barotropic experiments further confirm the notion that the striking differences in the atmospheric anomalies over North Atlantic and Eurasia (including northeast Asia) between the persistent and reverse years can be attributable to the distinct SST anomalies in the North Atlantic.

5. Summary and discussions

This study examines different evolutions of haze pollution over NCPR from

winter to the succedent spring according to the analyses based on observational data and reanalyses. It is found that interannual variation of haze pollution (as indicated by the DECC) over NCPR in winter has a marginal positive relation with that in the following spring, with a correlation coefficient of about 0.3 over 1980–2011 between the haze pollution index in winter and spring, significant at the 90% confidence level. This indicates that in most years when haze pollution over the NCPR is more (less) serious in winter, air condition in the following spring is also worse (better) than normal. Additionally, it is found that there appear some years when DECC anomalies in the following spring are significantly opposite to those in winter. We then focus on comparing atmospheric anomalies for the two types of years (i.e. persistent years and reverse years) to understand why there occur two completely different evolutions of haze pollution over the NCPR from winter to following spring, as schematically summarized in Fig. 14.

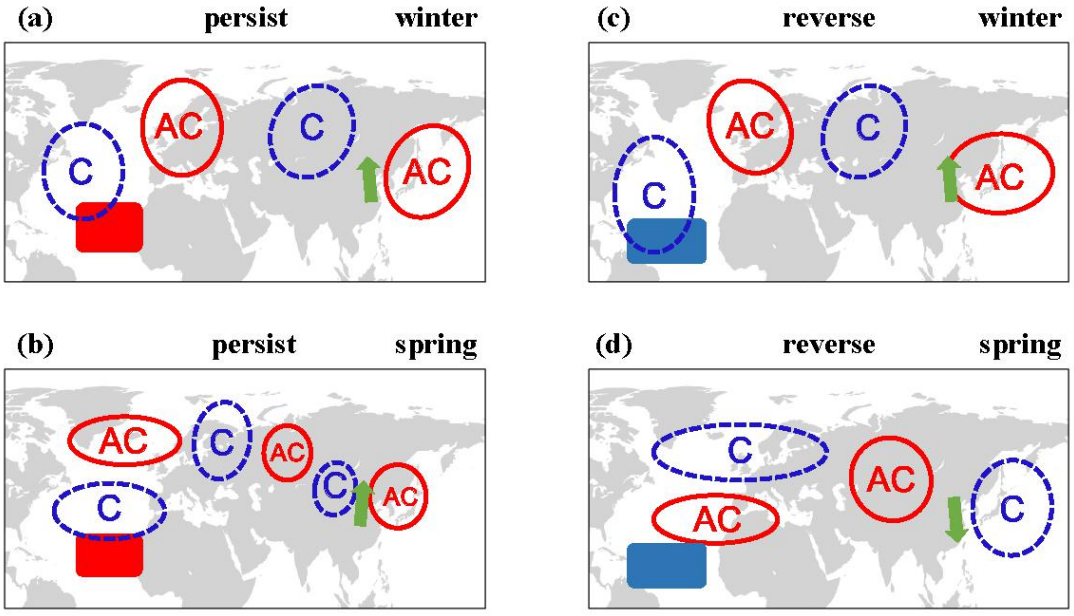

Figure 14. Schematic diagram showing evolutions of DECC, SST, and atmospheric circulation anomalies from winter to spring for (left column) the persistent cases and

716 (right column) the reverse cases. Red solid contours (blue dashed contours) indicate
717 anticyclonic circulation anomalies (cyclonic circulation anomalies). Red (blue)
718 shadings in the North Atlantic indicate positive (negative) SST anomalies.

719 In the persistent years, above-normal DECC (indicating more serious haze
720 pollution) over the NCPR could be maintained to the succedent spring (Figs. 14a and
721 14b). This is attributable to the persistence of the anticyclonic anomaly over northeast
722 Asia and associated southerly wind anomalies to its west side over the NCPR (Figs.
723 14a and 14b). The southerly wind anomalies over the NCPR oppose the
724 climatological mean northerly winds, reduce the surface wind speed and BLH, and
725 decrease the dispersion of the pollutants, which finally lead to more serious haze
726 pollution in winter and spring. In addition, the southerly wind anomalies carry wetter
727 and warmer air from lower latitude, and lead to increase in the relative humidity,
728 which are also conducive to haze pollution. As have been demonstrated by previous
729 studies, the increase in the relative humidity is conducive to the generation of
730 secondary organic compounds and secondary aerosol species, which also has an
731 important contribution to the occurrence of haze pollution event over NCPR (Yu et al.
732 2005; Hennigan et al. 2008). Formation of the anticyclonic anomaly over the
733 northeast Asia in winter is closely related to the EAWR teleconnection pattern, while
734 in spring it is related to the positive phase of spring NAO and warm SSTA in the
735 subtropical northeastern Atlantic (Fig. 14a).

736 In the reverse years, an anticyclonic anomaly also appears over northeast Asia
737 and associated southerly wind anomalies occur over NCPR in winter, which
738 contribute to above-normal DECC (Fig. 14c). In addition, formation of the anomalous

739 anticyclone over the northeast Asia is also related to the EAWR pattern (Fig. 14c).
740 However, in the following spring, northeast Asia is covered by cyclonic anomaly
741 which is related to the positive phase of the NAO and cold SSTA in the subtropical
742 North Atlantic (Fig. 14d), which is in sharp contrast to those in the persistent years.
743 The northerly wind anomalies over the NCPR to the west flank of the anomalous
744 cyclone result in decrease in the DECC over the NCPR via reduction of relative
745 humidity and increasing the surface wind speed (Fig. 14d).

746 The distinct evolutions of atmospheric anomalies over North Atlantic and
747 Eurasia (including northeast Asia) are found to be closely related to the different
748 evolutions of SSTA in the North Atlantic. In the persistent (reverse) years, positive
749 (negative) SSTA in the subtropical northeastern (northwestern) Atlantic are
750 maintained to the following spring due to the positive air-sea interaction process.
751 Then, positive (negative) spring SSTA in the subtropical North Atlantic contribute to
752 the formation of negative (positive) NAO-like pattern over North Atlantic and the
753 generation of anticyclonic (cyclonic) anomaly over northeast Asia, and the occurrence
754 of associated southerly (northerly) wind anomalies over the NCPR via atmospheric
755 Rossby wave train. Results of barotropic model simulations with three experiments
756 further confirm the observed findings.

757 In this study, we find that negative SSTA in the subtropical northwestern Atlantic
758 play an important role for the formation of the positive NAO-like atmospheric
759 anomaly in the reverse years. It seems that wintertime surface heat flux changes
760 induced by the EAWR-related atmospheric anomalies cannot fully explain the

761 formation of strong cold SSTA in the subtropical northwestern Atlantic. This suggests
762 that other factors may also be important for the formation of the negative SST
763 anomalies, which remain to be explored. Studies indicated that ENSO-related SSTA in
764 the tropical Pacific also has a strong impact on atmospheric anomalies over East Asia
765 and haze pollution over eastern China (Wang et al. 2000; Li et al. 2017; Zhang et al.
766 2017; He et al. 2019). We have examined evolutions of SSTA in the tropical Pacific
767 from winter to subsequent spring in the persistent and reverse years. Results show that
768 SSTA in the tropical Pacific related to ENSO are weak both in the persistent and
769 reverse years (not shown). This suggests that ENSO-related SSTA may not have a
770 contribution to the interannual variation of haze pollution over the NCPR, which is
771 consistent with a recent study by He et al. (2019). It is reported that ENSO-related
772 SSTA in the tropical Pacific has a significant impact on the haze pollution over
773 southern China. By contrast, impact of ENSO on the haze pollution over North China
774 is weak (He et al. 2019). Furthermore, previous studies indicated that Arctic sea ice
775 anomalies over Eurasia may also be important for the formation of the atmospheric
776 anomalies over East Asia in association with the haze pollution over north China
777 (Wang et al. 2015; Yin and Wang 2017). We have examined Arctic sea ice anomalies
778 in winter and spring for the persistent and reverse years. We find that sea ice
779 anomalies over most portions of Arctic are weak and statistically insignificant (results
780 not shown). This suggests that Arctic sea ice changes are not likely to have an
781 important role in the distinct evolutions of haze pollution from winter to subsequent
782 spring over the NCPR for the persistent and reverse years.

Code availability. Figures in this study are constructed with the NCAR Command Language (http://www.ncl.ucar.edu/). All codes used in this study are available from the corresponding author (S.C.).

Data availability: Atmospheric data are derived from the NCEP-NCAR reanalysis (http://www.esrl.noaa.gov/psd/data/gridded/data.ncep.reanalysis.html, last access: 6 February 2021) (NCEP-NCAR, 2021). SST data are obtained from the https://psl.noaa.gov/data/gridded/data.noaa.ersst.v5.html (last access: 6 February 2021) (NOAA, 2021). Atmospheric teleconnection indices are obtained from https://www.cpc.ncep.noaa.gov/data/teledoc/telecontents.shtml (last access: 6 February 2021) (CPC, 2021). Surface data of visibility and relative humidity can be obtained from the authors upon request.

Author contributions. Y.L. and C.S. designed the research, performed the analysis and wrote the paper. All the authors discussed the results and commented on the manuscript.

Competing Interests. The authors declare that they have no competing interests.

Acknowledgments. We thank two anonymous reviewers for their constructive suggestions and comments, which help to improve the paper. This work was

supported jointly by the National Natural Science Foundation of China (Grants 41721004 and 41961144025), and the Chinese Academy of Sciences Key Research Program of Frontier Sciences (QYZDY-SSW-DQC024).

Financial support. This research has been supported by the National Natural Science Foundation of China (Grants 41721004 and 41961144025), and the Chinese Academy of Sciences Key Research Program of Frontier Sciences (QYZDY-SSW-DQC024).

References

Cai, W.J., Li, K., Liao, H., Wang, H.J. and Wu, L.X.: Weather conditions conducive to Beijing severe haze more frequent under climate change, Nat. Clim. Change, 7, 257–263, 2017.

Chang, L., Xu, J., Tie, X., and Wu, J.: Impact of the 2015 El Niño event on winter air quality in China, Sci. Rep., 6, 34275, 2016.

Che, H., Zhang, X., Li, Y., Zhou, Z., Qu, J. and Hao, X.: Haze trends over the capital cities of 31 provinces in China, 1981–2005, Theor. Appl. Climatol., 97, 235–242, 2009.

Cheng, J., Su, J., Cui, T., Li, X., Dong, X., Sun, F., Yang, Y., Tong, D., Zheng, Y., Li, Y., Li, J., Zhang, Q., and He, K.: Dominant role of emission reduction in $PM_{2.5}$ air quality improvement in Beijing during 2013-2017: a model-based decomposition analysis, Atmos. Chem. Phys., 19, 6125-6146, 2019.

Chen, G. S., and Huang, R. H.: Excitation mechanisms of the teleconnection patterns affecting the July precipitation in Northwest China, J. Climate, 25, 7834–7851, 2012.

Chen, S., Wu, R., and Chen, W.: The changing relationship between interannual variations of the North Atlantic Oscillation and northern tropical Atlantic SST, J. Clim., 28, 485–504, 2015.

Chen, S., Wu, R., and Liu, Y.: Dominant modes of interannual variability in Eurasian surface air temperature during boreal spring, J. Clim., 29, 1109–1125, 2016.

Chen, S., Guo, J., Song, L., Li, J., Liu, L., and Cohen, J.: Interannual variation of the

835 spring haze pollution over the North China Plain: Roles of atmospheric
836 circulation and sea surface temperature, Int. J. Climatol., 39, 783-798, 2019.
837 Chen, S., Guo, J., Song, L., Cohen, J., and Wang, Y.: Temporal disparity of the
838 atmospheric systems contributing to interannual variation of wintertime haze
839 pollution in the North China Plain, Int. J. Climatol., 40,128-144, 2020.
840 Cohen, A., Brauer, M., Burnett, R., Anderson, H., Frostad, J., Estep, K., Balakrishnan,
841 K., Brunekreef, B., Dandona, L., Dandona, R., Feigin, V., Freedman, G., Hubbell,
842 B., Jobling, A., Kan, H., Knibbs, L., Liu, Y., Martin, R., Morawska, L., Pope, C.,
843 Shin, H., Straif, K., Shaddick, G., Thomas, M., Dingenen, R., Donkelaar, A., Vos,
844 T., Murray, C., and Forouzanfar, M.: Estimates and 25-year trends of the global
845 burden of disease attributable to ambient air pollution: An analysis of data from
846 the Global Burden of Diseases Study 2015, Lancet, 389, 1907–1918, 2017.
847 Craig, C.D. and Faulkenberry, G.D.: The application of ridit analysis to detect trends
848 in visibility, Atmos. Environ., 13, 1617–1622, 1979.
849 Czaja, A., and Frankignoul, C.: Influence of the North Atlantic SST on the
850 atmospheric circulation, Geophys. Res. Lett., 26, 2969–2972, 1999.
851 Czaja, A., and Frankignoul, C.: Observed impact of Atlantic SST anomalies on the
852 North Atlantic oscillation, J. Climate, 15, 606–623, 2002.
853 Czaja, A., Robertson, A.W., and Huck, T.: The role of Atlantic ocean–atmosphere
854 coupling in affecting North Atlantic Oscillation variability. The North Atlantic
855 Oscillation: Climatic Significance and Environmental Impact, J. W. Hurrell, Eds.,
856 Geophys. Monogr., Vol. 134, Amer. Geophys. Union, 147–172, 2003.

857 CPC: Climate Prediction Center atmospheric teleconnections, available at:
858 http://www.esrl.noaa.gov/psd/data/gridded/data.noaa.ersst.v5.html, last access: 6
859 February 2021. https://www.cpc.ncep.noaa.gov/data/teledoc/telecontents.shtml,
860 last access: 6 February 2021.
861 Dang, R., and Liao, H.: Severe winter haze days in the Beijing–Tianjin–Hebei region
862 from 1985 to 2017 and the roles of anthropogenic emissions and meteorology,
863 Atmos. Chem. Phys., 19, 10801–10816, 2019.
864 Ding, Y.H. and Liu, Y.J.: Analysis of long-term variations of fog and haze in China in
865 recent 50 years and their relations with atmospheric humidity, Sci. China Earth
866 Sci., 57, 36–46, 2014.
867 Ding, Y., Wu, P., Liu, Y., and Song, Y.: Environmental and dynamic conditions for the
868 occurrence of persistent haze events in North China, Engineering 3, 266–271,
869 2017.
870 Duan, W., Song, L., Li, Y. and Mao, J. Modulation of PDO on the predictability of the
871 interannual variability of early summer rainfall over South China, J. Geophys.
872 Res., 118, 1–14, 2013.
873 Fu, G.Q., Xu, W.Y., Yang, R.F., Li, J.B. and Zhao, C.S.: The distribution and trends of
874 fog and haze in the North China plain over the past 30 years, Atmos. Chem.
875 Phys., 14, 11949–11958, 2014.
876 Gao, H., and Li, X.: Influences of El Niño Southern Oscillation events on haze
877 frequency in eastern China during boreal winters, Int. J. Climatol., 35,
878 2682–2688, 2015.

879 Guo, J.P., Su, T., Li, Z., Miao, Y., Li, J., Liu, H., Xu, H., Cribb, M. and Zhai, P.:
880 Declining frequency of summertime local-scale precipitation over eastern China
881 from 1970 to 2010 and its potential link to aerosols, Geophys. Res. Lett., 44,
882 5700–5708, 2017.
883 Guo, J., Liu, H., Li, Z., Rosenfeld, D., Jiang, M., Xu, W., Jiang, J. H., He, J., Chen, D.,
884 Min, M., and Zhai, P.: Aerosol-induced changes in the vertical structure of
885 precipitation: a perspective of TRMM precipitation radar, Atmos. Chem. Phys.,
886 18, 13329–13343, 2018.
887 He, C., Liu, R., Wang, X., Liu, S.C., Zhou, T., and Liao, W.: How does El
888 Niño-Southern Oscillation modulate the interannual variability of winter haze
889 days over eastern China? Sci. Total Environ., 651, 1892–1902, 2019.
890 Hennigan, C.J., Bergin, M.H., Dibb, J.E.,and Weber, R.J.: Enhanced secondary
891 organic aerosol formation due to water uptake by fine particles, Geophys. Res.
892 Lett., 35(18), 2008.
893 Hodson, D. L. R., Sutton, R. T., Cassou, C., Keenlyside, N., Okumura, Y., and Zhou,
894 T. J.: Climate impacts of recent multidecadal changes in Atlantic Ocean sea
895 surface temperature: A multimodel comparison, Clim. Dyn., 34, 1041–1058,
896 2010.
897 Hu, Z.-Z., and Huang, B.: On the significance of the relationship between the North
898 Atlantic Oscillation in early winter and Atlantic sea surface temperature
899 anomalies, J. Geophys. Res., 111, D12103, 2006.
900 Huang, B., and Shukla, J.: Ocean–atmosphere interactions in the tropical and

subtropical Atlantic Ocean. J. Clim., 18, 1652–1672, 2005.

Huang B, and Coauthors.: Extended reconstructed sea surface temperature, version 5 (ERSSTv5): Upgrades, validations, and intercomparisons, J. Clim., 30, 8179–8205, 2017.

Hurrell, J. W.: Decadal trends in the North Atlantic Oscillation. Science, 269, 676–679, 195

Kalnay, E., Kanamitsu, M., Kistler, R., Collins, W., Deaven, D., Gandin, L., Iredell, M., Saha, S., White, G., Woollen, J., Zhu, Y., Leetmaa, A., Reynolds, R., Chelliah, M., Ebisuzaki, W., Higgins, W., Janowiak, J., Mo, K.C., Ropelewski, C., Wang, J., Jenne, R. and Joseph, D.: The NCEP/NCAR 40-year reanalysis project, Bull. Amer. Meteor. Soc., 77, 437–471, 1996.

Kerr, R.A.: A North Atlantic climate pacemaker for the centuries, Science, 288, 1984–1986, 2000.

Koren, I., Altaratz, O., Remer, L.A., Feingold, G., Martins, J.V. and Heiblum, R. H.: Aerosol-induced intensification of precipitation from the Tropics to the mid-latitudes, Nat. Geosci., 5, 118–122, 2012.

Koschmieder, H.: Theorie der horizontalen Sichtweite Beit. Physics of the Atmosphere, 12, 33–55, 1926.

Krishnamurti, T. N., Stefanova, L., and Misra, V.: Tropical Meteorology: An Introduction. Springer-Verlag, 424 pp, 2013:

Li, J., Li, C. and Zhao, C.: Different trends in extreme and median surface aerosol extinction coefficients over China inferred from quality-controlled visibility data,

923 Atmos. Chem. Phys., 18, 3289–3298, 2018.
924 Li, Q., Zhang, R. and Wang, Y.: Interannual variation of the wintertime fog-haze days
925 across central and eastern China and its relation with East Asian winter monsoon,
926 Int. J. Climatol., 36, 346–354, 2016.
927 Li, T., Wang, B., Wu, B., and Zhou, T.: Theories on formation of an anomalous
928 anticyclone in Western North Pacific during El Niño: a review, J. Meteorol. Res.
929 31, 987–1006, 2017.
930 Li, X., Yu, C., Deng, X., He, D., Zhao, Z., Mo, H., Mo, J., and Wu, Y.: Mechanism for
931 synoptic and intra-seasonal oscillation of visibility in Beijing-Tianjin-Hebei
932 region, Theor. Appl. Climatol., 2020.
933 Liu, T., Gong, S., He, J., Yu, M., Wang, Q., Li, H., et al.: Attributions of
934 meteorological and emission factors to the 2015 winter severe haze pollution
935 episodes in China's Jing-Jin-Ji area, Atmos. Chem. Phys. 17, 2971–2980, 2017.
936 Lu, X., Lin, C., Li, W., Chen, Y., Huang, Y., Fung, J., and Lau, A.: Analysis of the
937 adverse health effects of $PM_{2.5}$ from 2001 to 2017 in China and the role of
938 urbanization in aggravating the health burden, Sci. Total Environ., 652, 683–695,
939 2019.
940 Ma, J., and Zhang, R.: Opposite interdecadal variations of wintertime haze occurrence
941 over North China Plain and Yangtze River Delta regions in 1980-2013, Sci. Total
942 Environ., 732, 139240, 2020.
943 Mantua, N.J., Hare, S.R., Zhang, Y., Wallace, J.M. and Francis, R.C.: A Pacific
944 interdecadal climate oscillation with impacts on salmon production, Bull. Amer.

945 Meteor. Soc., 78, 1069–1079, 1997.
946 NCEP-NCAR, Monthly and daily mean atmospheric reanalysis data, available at:
947 http://www.esrl.noaa.gov/psd/data/gridded/data.ncep.reanalysis.html, last access:
948 6 February 2021.
949 NOAA: NOAA Extended Reconstructed Sea Surface Temperature (SST) V5 data sets,
950 available at: http://www.esrl.noaa.gov/psd/data/gridded/data.noaa.ersst.v5.html,
951 last access: 6 February 2021.
952 O'Reilly, C. H., Woollings, T., and Zanna, L.: The impact of tropical precipitation on
953 summertime Euro-Atlantic circulation via a circumglobal wave train, J. Clim., 31,
954 6481–6504, 2018.
955 Pan, L.-L.: Observed positive feedback between the NAO and the North Atlantic
956 SSTA tripole, Geophys. Res. Lett., 32, L06707, 2005.
957 Peng, S., Robinson, W. A., and Li, S.: Mechanisms for the NAO responses to the
958 North Atlantic SST tripole, J. Clim., 16, 1987–2004, 2003.
959 Rodwell, M. J., and Folland, C. K.: Atlantic air–sea interaction and seasonal
960 predictability, Quart. J. Roy. Meteor. Soc., 128, 1413–1443, 2002.
961 Rosenfeld, D., Dai, J., Yu, X., Yao, Z., Xu, X., Yang, X. and Du, C.: Inverse relations
962 between amounts of air pollution and orographic precipitation, Science,
963 315(5817), 1396–1398, 2007.
964 Sardeshmukh, P. D., and Hoskins, B. J.: The generation of global rotational flow by
965 steady idealized tropical divergence, J. Atmos. Sci., 45, 1228–1251, 1988.
966 Sun, C., Li, J. P., and Zhao, S. Remote influence of Atlantic multidecadal variability

967 on Siberian warm season precipitation, Sci. Rep., 5, 16853, 2015.
968 Takaya, K. and Nakamura, H.: A formulation of a phaseindependent wave activity
969 flux for stationary and migratory quasigeostrophic eddies on a zonally varying
970 basic flow, J. Atmos. Sci., 58, 608–627, 2001.
971 Tie, X., Huang, R. and Dai, W.: Effect of heavy haze and aerosol pollution on rice and
972 wheat productions in China, Sci. Rep., 6, 29612, 2016.
973 Ting, M. F.: Steady linear response to tropical heating in barotropic and baroclinic
974 models, J. Atmos. Sci., 53, 1698–1709, 1996.
975 Visbeck, M., Chassignet, E., Curry, R., and Delworth, T.: The ocean's response to
976 North Atlantic variability. The North Atlantic Oscillation, J. Hurrell et al., Eds.,
977 Geophys. Monogr., Vol. 134, Amer. Geophys. Union, 113–145, 2003.
978 Wang, B., Wu, R.G. and Fu, X.H.: Pacific–East Asian teleconnection: how does
979 ENSO affect East Asian climate? J. Clim., 13, 1517–1536, 2000.
980 Wang, F., Guo, J., Wu, Y., Zhang, X., Deng, M., Li, X., Zhang, J. and Zhao, J.:
981 Satellite observed aerosol-induced variability in warm cloud properties under
982 different meteorological conditions over eastern China, Atmos. Environ., 84(2),
983 122–132, 2014a.
984 Wang, H.J. and Chen, H.P.: Understanding the recent trend of haze pollution in
985 Eastern China: roles of climate change, Atmos. Chem. Phys., 16, 420–421, 2016.
986 Wang, L., Liu, Y., Zhang, Y., Chen, W., and Chen, S.: Time-varying structure of the
987 wintertime Eurasian pattern: Role of the North Atlantic sea surface
988 temperature and atmospheric mean flow, Clim Dynam., 52, 2467–2479, 2019.

989 Wang, X., Wei, W., Cheng, S., Li, J., Zhang, H., Lv, Z.: Characteristics and
990 classification of PM2. 5 pollution episodes in Beijing from 2013 to 2015. Sci.
991 Total Environ., 612, 170–179, 2018.
992 Wang, Y., Zhang, R. and Saravanan, R.: Asian pollution climatically modulates
993 mid-latitude cyclones following hierarchical modeling and observational analysis,
994 Nature Communications, 5, 3098, 2014b.
995 Watanabe, M.: Asian jet waveguide and a downstream extension of the North Atlantic
996 Oscillation, J. Clim., 17, 4674–4691, 2004.
997 Wu, G., Li, Z.–.Q., Fu, C., Zhang, X., Zhang, R.–.Y., Zhang, R., Zhou, T., Li, J., Li, J.,
998 Zhou, D.,Wu, L., Zhou, L., He, B., and Huang, R. Advances in studying
999 interactions between aerosols and monsoon in China, Sci. China Earth Sci. 59,
1000 1–16, 2016.
1001 Wu, L., and Liu, Z.: NorthAtlantic decadal variability: Air–sea coupling,
1002 oceanicmemory, and potential Northern Hemisphere resonance, J. Clim., 18,
1003 331–349, 2005.
1004 Wu, R., Yang, S., Liu, S., Sun, L., Lian, Y., and Gao, Z.: Northeast China summer
1005 temperature and North Atlantic SST, J. Geophys. Res., 116, D16116, 2011.
1006 Wu, Z., Wang, B., Li, J., and Jin, F.-F.: An empirical seasonal prediction model of the
1007 East Asian summer monsoon using ENSO and NAO, J. Geophys. Res., 114,
1008 D18120, 2009.
1009 Xiao, D., Li, Y., Fan, S., Zhang, R., Sun, J. and Wang, Y.: Plausible influence of
1010 Atlantic Ocean SST anomalies on winter haze in China, Theor. Appl. Climatol.,

1011 122, 249–257, 2014.
1012 Yin, Z., Wang, H., and Guo, W.: Climatic change features of fog and haze in winter
1013 over North China and Huang-Huai Area, Sci. China Earth Sci., 58, 1370–1376,
1014 2015.
1015 Yin, Z. and Wang, H.: Role of atmospheric circulations in haze pollution in December
1016 2016, Atmos. Chem. Phys., 17, 11673–11681, 2017.
1017 Yin, Z. and Wang, H.: The strengthening relationship between Eurasian snow cover
1018 and December haze days in central North China after the mid-1990s, Atmos.
1019 Chem. Phys., 18, 4753–4763, 2018.
1020 Yu, J.Z., Huang, X.F., Xu, J., and Hu, M.: When aerosol sulfate goes up, so does
1021 oxalate: implication for the formation mechanisms of oxalate, Environ. Sci.
1022 Technol., 39(1), 128–133, 2005.
1023 Zhang, J., Liu, J., Ren, L., Wei, J., Duan, J., Zhang, L., Zhou, X., and Sun, Z.: PM2.5
1024 induces male reproductive toxicity via mitochondrial dysfunction, DNA damage
1025 and RIPK1 mediated apoptotic signaling pathway, Sci. Total Environ., 634,
1026 1435–1444, 2018.
1027 Zhang, Q. and Crooks, R.: Toward an environmentally sustainable future: Country
1028 environmental analysis of the People's Republic of China, China Financial and
1029 Economic Publishing House, Beijing, 2012.
1030 Zhang, R.H., Min, Q.Y. and Su, J.Z. Impact of El Niño on atmospheric circulations
1031 over East Asia and rainfall in China: role of the anomalous western North Pacific
1032 anticyclone, Sci. China Earth Sci., 60, 1124–1132, 2017.

1033 Zhang, X., Huang, Y., Zhu, W., and Rao, R. Aerosol characteristics during summer
1034 haze episodes from different source regions over the coast city of North China
1035 Plain, J. Quant. Spectrosc. Radiat. Transf., 122, 180–193, 2013.
1036 Zhang, Y., Yin, Z., and Wang, H. Roles of climate variability on the rapid increase of
1037 winter haze pollution in north China after 2010, Atmos. Chem. Phys., pp 1–19,
1038 2020.
1039 Zhang, Y., Wallace, J.M. and Battisti, D.S.: ENSO-like interdecadal variability:
1040 1900–93, J. Climate, 10, 1004–1020, 1997.
1041 Zhang, Z., Zhang, X., Gong, D., Kim, S.J., Mao, R., and Zhao, X.: Possible influence
1042 of atmospheric circulations on winter haze pollution in the
1043 Beijing–Tianjin–Hebei region, northern China, Atmos. Chem. Phys., 16,
1044 561–571, 2016.
1045 Zhao, W., Chen, S., Chen, W., Yao, S., Nath, D., and Yu, B.: Interannual variations of
1046 the rainy season withdrawal of the monsoon transitional zone in China, Clim.
1047 Dynam., 53, 2031-2046, 2019.
1048 Zhao, S., Li, J., and Sun, C.: Decadal variability in the occurrence of wintertime haze
1049 in central eastern China tied to the Pacific Decadal Oscillation, Sci. Rep., 6,
1050 27424, https://doi.org/10.1038/srep27424, 2016.
1051 Zuo, J., Li, W., Sun, C., Xu, L., and Ren, H.: Impact of the North Atlantic sea surface
1052 temperature tripole on the East Asian summer monsoon, Adv. Atmos. Sci., 30,
1053 1173–1186, 2013.
1054